Thermal excitation and decay of nuclei from antiproton-nucleus interactions at 1.22 GeV

B. Lott,[1,*] F. Goldenbaum,[2,†] A. Böhm,[1] W. Bohne,[2] T. von Egidy,[3] P. Figuera,[2,‡] J. Galin,[1] D. Hilscher,[2] U. Jahnke,[2] J. Jastrzebski,[4] M. Morjean,[1] G. Pausch,[5] A. Péghaire,[1] L. Pienkowski,[2,4] D. Polster,[2] S. Proschitzki,[6] B. Quednau,[1] H. Rossner,[2] S. Schmid,[3] and W. Schmid[3]

[1]*GANIL (IN2P3-CNRS, DSM-CEA), F-14076 Caen Cedex 5, France*
[2]*Hahn-Meitner-Institut, Glienickerstrasse 100, D-14109 Berlin, Germany*
[3]*TU-München, D-85748 Garching, Germany*
[4]*Heavy Ion Laboratory, Warsaw University, 02-093 Warszawa, Poland*
[5]*FZ-Rossendorf, D-01314 Dresden, Germany*
[6]*IPN Orsay, F-91406 Orsay, France*
(Received 27 June 2000; published 21 February 2001)

The formation and subsequent decay of nuclei excited via the annihilation of 1.22-GeV antiprotons have been investigated at the low energy antiproton ring (LEAR). Both neutrons and charged products, from protons up to fission fragments and heavy residues, were detected over a solid angle of 4π by means of the Berlin neutron ball (BNB) and the Berlin silicon ball (BSiB), respectively. All events associated with an inelasticity greater than 10 MeV were recorded, a condition fulfilled for 100% of the annihilation events. The distributions of excitation energy (E^*) of the transient hot nuclei have been investigated for a large range of target nuclei, E^* being determined event by event from the total multiplicity of light particles. The average excitation energies are about twice as large as for annihilations at rest, and range from 2.5 MeV/nucleon for the Cu target to 1.5 MeV/nucleon for the U target, in good agreement with the predictions of an intranuclear-cascade model. The distributions extend to $E^*>8$ MeV/nucleon for Cu and $E^*>5$ MeV/nucleon for Au, with cross sections exceeding 1% of σ_{reac}. Thanks to the capability of determining E^* for all events, largely irrespective of their mass partitions, the probabilities of the different decay channels at play could be estimated as a function of E^*. The data show the prevalence of fission and evaporation up to $E^*=4–5$ MeV/nucleon for Au and U. The fission probability P_{fis} was measured for the first time over the full range of E^*. The reproduction of the data by statistical models is reasonable, provided that the ratio a_f/a_n is adjusted for the different targets and a transient time shorter than 1×10^{-21} s is considered. The experiment has allowed the fission probability to be investigated as functions of the associated neutron and light-charged particle multiplicities. The intermediate-mass fragment multiplicities rise smoothly with E^* up to about 1 unit at $E^*=1$ GeV for Au and U, with no indication of significant contribution from another process than evaporation. Heavy residues have been measured quite abundantly at the highest E^*, with most of their kinetic energy arising from the recoil effects in the evaporation stage. Overall, the data allow a coherent picture to be established, consistent with the hot nucleus retaining conventional decay properties.

PACS number(s): 25.43.+t, 24.60.Dr, 24.75.+i

I. INTRODUCTION

The behavior of strongly heated nuclei and the prospect of reaching the maximal or ''limiting'' temperature that nuclei can sustain [1,2] have been a subject of great interest for the last decade. The advent of medium-energy heavy-ion beams (several tens of MeV/nucleon) and relativistic-energy beams (hundreds or thousands of MeV/nucleon) has raised expectations that nuclei could easily be led to thermal energies approaching or even exceeding their binding energies and that a new field of investigation could thus open up. However, it quickly became evident that in medium- or high-energy nucleus-nucleus collisions, the nuclei also experience collective excitations strongly favored by their large masses. Nuclei are compressed, deformed, and subject to transfers of orbital angular momentum into intrinsic spin, with the importance of all three collective effects being strongly dependent on the masses of the nuclei, the bombarding energy, and the impact parameter. Investigating the effects of nuclear temperature from such nuclei becomes a challenge when several collective degrees of freedom are simultaneously at play. Indeed, the latter can strongly influence the decay pattern of the nucleus and ultimately mask the sought-after thermal effects. Moreover, the presence of several heated nuclei in a single event—a projectilelike and a targetlike nucleus with sometimes additional intermediate-velocity fragments built from parts of them—makes the experimental characterization of the different products extremely tedious, if at all possible.

In order to circumvent the above mentioned difficulties, the thermal energy should not be brought in from a massive projectile but rather from a light one: a GeV or multi-GeV hadron. As shown in several model calculations [3–7] a light

63 034616-1

projectile, in particular a shower of pions from antiproton annihilation, generates neither much compression, nor much spin, nor strong deformation, although a substantial amount of thermal energy (about 1 GeV) can be generated on a very short time-scale (30 fm/c) in the impinged nucleus. Moreover, the problem of dealing with multiple hot nuclei in a single event simply vanishes, making the data analysis more straightforward.

The entire heating process in antiproton-annihilation reactions can be modeled [5,7] by considering an intranuclear cascade (INC), with all elementary processes associated with probabilities derived from free meson and baryon interactions. At high bombarding energy, due to the boost imparted to the freed pions arising from momentum conservation, a large fraction of the created pions interact simultaneously with the nucleus, leading to higher energy depositions than when following annihilation at rest. The present investigation has been limited to the highest antiproton energy of 1.22 GeV available at the low energy antiproton ring (LEAR) at CERN. It must be stressed that, when the present experiment was performed, there were rather few investigations involving energetic antiproton nucleus reactions [8–13] as compared to those involving antiproton-nucleus at rest. Since then, another experiment [14] has been performed.

The aim of the study was twofold: to investigate both the ability of energetic antiprotons to heat up nuclei and to study their decay properties over a broad range of excitation energies in great detail, with some emphasis on fission. To our knowledge, this is the first time that a fission study has been made over such a large range of excitation energies (up to about 1 GeV) and with different target materials (Au, U) under very exclusive experimental conditions. Indeed, not only the excitation energy is inferred on an event-by-event basis, but the numbers of accompanying light charged particles (LCPs), neutrons, and intermediate mass fragments (IMFs) are also measured. As it will be shown for the U target in particular, for a given excitation energy there exists a strong correlation between the fission probability and the ratio of the numbers of emitted neutrons and LCPs.

The observed decay properties have been confronted with the predictions of the statistical model, the characteristics of the transient primary nuclei being modeled with an INC model. The fission probability gives direct access to the saddle time when most of the other experimental approaches are only sensitive to the scission time [15,16]. Also, because of the broad range of excitation energies involved and thus the broad range of emission times, the investigation of the so-called transient time for fission is made possible in a much broader domain than before [17].

The paper is organized as follows. In a first section, the characteristics of the annihilation process will be reviewed and the comparison with other approaches (proton- and heavy ion-induced reactions) will be examined. After a description of the experimental setup, the obtained data will be presented. The method used for inferring the excitation energy of the struck nucleus after energy relaxation on an event-by-event basis will then be discussed. The heating capability of the 1.22-GeV antiprotons on different nuclei will be reviewed and compared with model predictions. Finally

the decay properties of the hot, heavy nuclei will be reviewed as a function of the thermal energy deposited and their fissility. The whole paper will then be summarized and some prospects given.

Partial accounts of the present results concerning the excitation energy distributions have already been published in Ref. [18], concerning the total fission cross sections in Ref. [19] and the decay modes of heavy nuclei, fission, and heavy residue formation in Ref. [20]. The results concerning the decay properties of light nuclei (Cu,Ag) where multifragmentation and even vaporization have been observed [21] due to the attainment of high excitation energy per nucleon will not be detailed here.

II. BASIC FEATURES OF ANTIPROTONIC HEATING OF NUCLEI

The most interesting features of the heating of nuclei using low-energy antiprotons are the following.

(i) Their ''softness'' and short associated time scale: The thermalization process is mediated through several pions that are emitted after annihilation of the antiproton. These pions are the main mediators of the energy deposition through their absorption and the excitation of the delta resonance. As the pion momenta are comparable with the intrinsic nucleon momenta, the expression ''radiationlike heating'' [22] appears appropriate. In order to maintain the ''softness'' of the heating process, it is desirable to keep the momentum of the incident particle as low as possible while the focusing of the pion cloud into the nucleus calls for high velocities. The present antiproton energy 1.22 GeV might represent an optimal compromise.

According to some calculations [4], it does not take more than 30 fm/c for the thermal equilibrium to be reached. If such a short time is also essentially involved in GeV proton- or pion-induced collisions [23], it takes much longer to reach thermal equilibrium in a heavy nucleus-nucleus collision at several tens of MeV per incident nucleon [24]. It must be remembered that the characteristic evaporation time of a nucleus of mass 200 at $E^* = 500$ MeV is about 30 fm/c and that achieving thermal relaxation very promptly is a decisive advantage. Only little cooling is expected to take place during the thermalization stage.

(ii) The minimization of collective excitations as shown by INC simulations [7,25]. As already pointed out, this is a distinctive aspect of light projectiles and of antiprotons in particular, provided that the initial momentum is not too large. The struck nucleus is not imparted any appreciable compression, deformation, or rotation in contrast to what is achieved in heavy nucleus-nucleus collisions.

(iii) The relatively low loss of mass and charge of the target nucleus during the heating stage. This is a difficult requirement to be fulfilled in heavy-ion (HI) induced reactions as exemplified in [26]. In order to explore broad ranges of excitation energy and temperature, the authors had to deal with an extended variety of nuclei with masses ranging from $A = 200$ down to $A = 50$. This drawback is strongly minimized in antiproton-induced reactions as shown from INC calculations giving the average mass and charge of the
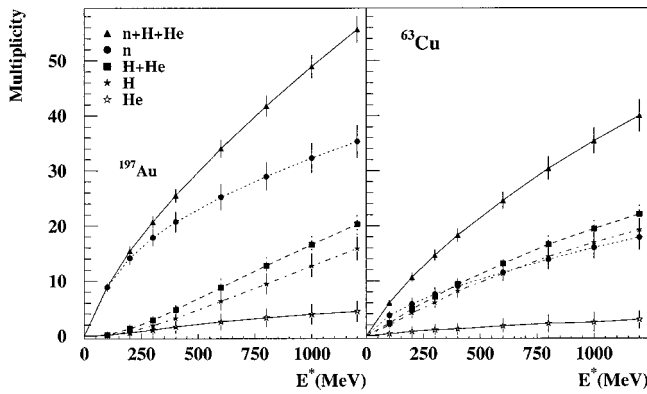
FIG. 1. Average multiplicities of different light particles evaporated from Au and Cu as calculated by GEMINI. The error bars correspond to the full width at half maximum (FWHM).

FIG. 2. Relative resolution $\Delta E^*/E^*$ of the excitation energy determination using the multiplicities of evaporated neutrons (n), light charged particles (LCP) or all light particles (LP=LCP+n) as calculated with GEMINI. ΔE^* was deduced from the FWHM of the corresponding particle multiplicity distributions. The calculation was performed without including the effect of the detection efficiency.

nucleus as a function of the excitation energy, which is reached at thermal equilibrium [7]. When ''preparing'' nuclei with $E^*=1$ GeV from a U target, seven charge units and 23 mass units are lost on average during the INC stage. It can also be shown that the spin generated in such reactions remains feeble (about 20 $\hbar$ units for a U target) and is very weakly dependent on the excitation energy above $E^*=100$ MeV. This is not the case in heavy-ion induced reactions when the available angular momentum in the entrance channels often exceeds thousands of $\hbar$ units [27]. Even if a small fraction of this huge amount is to be found as intrinsic spin of the excited nuclei, this represents nevertheless much larger spins than the ones involved in antiproton-induced reactions.

As stressed in a previous paper [18], the excitation energy distribution as obtained from the INC model calculation is rather broad and extends to values up to 1 GeV for massive targets. One of the aims of the present experiment was to check these predictions and this task has been done for a series of target nuclei: ^{12}C, ^{nat}Cu, ^{89}Y, ^{92}Mo, ^{100}Mo, ^{nat}Ag, ^{nat}Sn, ^{165}Ho, ^{197}Au, ^{209}Bi, and ^{238}U. For this purpose a simple procedure has been adopted in order to infer event by event the thermal energy. It is based on the fact—substantiated by an evaporation code [28]—that the energy is essentially removed by neutron and light charged particle emission as exemplified in Fig. 1 for two different target nuclei. The final fate of the nucleus (splitting into two fragments, as in binary fission, or more fragments, or no splitting at all when an evaporation residue remains) has only a minor impact on the number of emitted light particles. When observing both, the evaporation of neutrons and of LCPs, the total number of these particles is the most relevant quantity to be considered as shown in Fig. 2, leading to a resolution in the E^* determination of about $\pm7\%$ (which, however doubles to approximately $\pm15\%$ when the actual detection efficiencies for neutrons and LCPs are taken into account). Considering the number of either only neutrons or only LCPs would lead to poorer resolutions. There is thus a definite improvement in using *both* neutrons and charged particles measured with high efficiencies ($>80\%$ for both). In order to ameliorate further this determination, one would need a kinetic energy measurement for each emitted particle, which
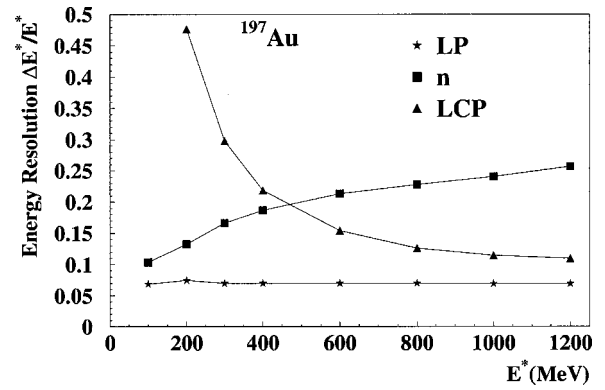
the present neutron detector cannot provide. Neglecting the IMFs in the described procedure has no significant impact on the gross E^* distribution in so far as their measured multiplicity is on average very low. It is only for rather rare events (mostly for light- or medium-mass targets) that the presence of several IMFs in the same event justifies to take them into consideration in the energy balance [21]. However the lack of kinetic energy measurement of the neutrons as well as the rather crude identification of the IMFs (and thus of their binding energy) make it difficult to assess E^* in a more accurate approach anyway. For this reason, in the present paper, we rather prefer disregarding the IMFs in the excitation energy balance in such a way that the data for all target nuclei are presented in a homogeneous way.

III. EXPERIMENTAL ARRANGEMENT AND DATA EVALUATION

The experiment PS208 was performed at LEAR at the maximum available energy of 1.22 GeV and with a beam intensity of about 10^5 particles per second delivered in a continuous way. The beam was tagged 16 m upstream by means of a 2-mm-thick, 6 cm $\times 2$ cm plastic scintillator (referred to as START in the following). Off-axis particles were vetoed by an annular plastic scintillator detector, placed close to START, and a set of detectors positioned in front of the neutron ball, inside and outside the beam pipe. The antiprotons were focused onto targets of 1–2 mg/cm^2 areal density, deposited on a 0.2-mm-thick Al frame (20 mm in diameter). The noncorrelated background was measured in runs with an empty frame in place of the target. The beam was stopped in a shielded beam dump, 10 m downstream of the target.

A shorter run was also performed with antiprotons at rest: the initial momentum of 200 MeV/c was degraded by means of a movable, tapered moderator whose position was set so as to maximize the annihilation rate in the target foil. The particle-tagging detector, 6 mm in diameter, was positioned
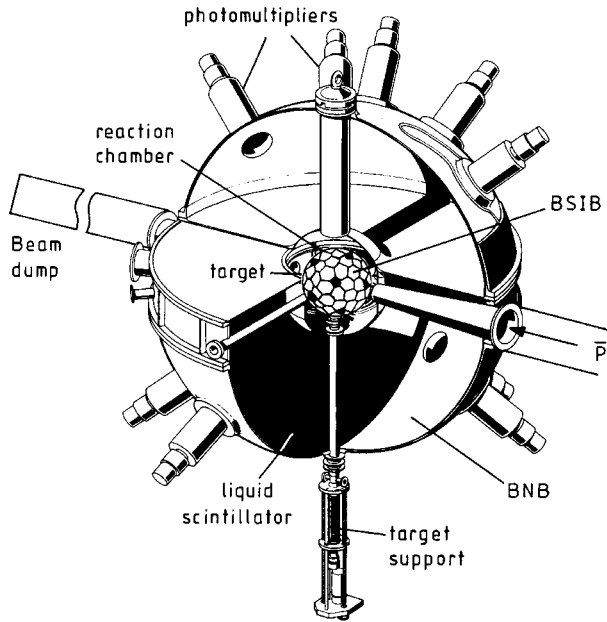
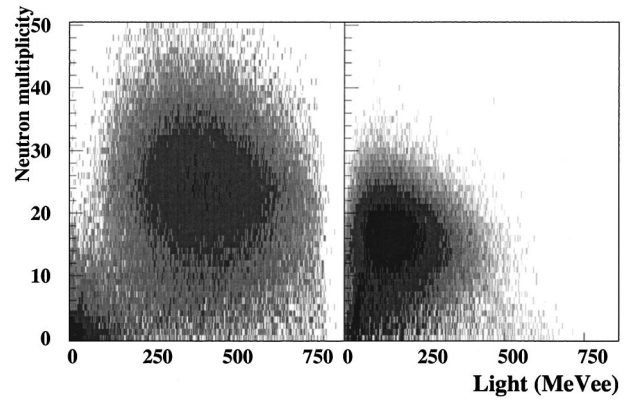FIG. 3. Schematical view of the experimental setup.

FIG. 4. Experimental yield plotted as functions of the prompt-light amplitude and the neutron multiplicity, as measured with a 2-mm-thick Pb target for 1.22-GeV antiproton (left) or proton (right) beams.

inside the silicon ball described in the following, at a distance of 2 cm from the target.

Figure 3 displays a schematic view of the experimental setup. The reaction products were detected by means of two concentric 4π sr detectors: the Berlin neutron ball (BNB) containing in its central part the Berlin silicon ball (BSiB) [29]. The target, standing at their common center, was mounted on a movable, very thin aluminum target ladder in order to minimize the shadowing for charged particles.

The BNB is a spherical tank with an outer diameter of 140 cm, housing a 40-cm-in-diameter scattering chamber and filled with 1.5 m^3 of liquid scintillator NE343, loaded with gadolinium, 0.5% in weight. The light signals are read out through 24 fast 4-in. phototubes mounted at the surface of the tank. This detector generates two types of signals with different time scales [30]. First, a so-called prompt signal is emitted within tens of nanoseconds, whenever a nuclear reaction takes place and emitted particles of any kind—charged particles or neutrons, or γ rays—propagate through the scintillator tank. This prompt signal is fed into the trigger and allows the whole inelastic reaction cross section to be measured. Due to the large annihilation cross section and the associated production of pions, the latter are the main contributors to this prompt light flash.

The delayed light flashes occur after the thermalization of the neutrons, their diffusion within the scintillator and their final capture by the Gd and H nuclei. The time spread of these captures over several tens of microseconds allows the counting of neutrons [30]. The so-called correlated background measured on-line in a second, 44-μs wide gate arbitrarily issued 400 μs after the first counting gate, amounted to 0.7 count in the neutron gate. It was subtracted from the multiplicity distribution via a standard deconvolution procedure. The detection efficiency [30], checked with the $\langle E \rangle$ = 2.1 MeV neutrons of a Cf source, amounts to 85% at this energy and decreases steadily for higher neutron energies

(40%, 25%, and 15% for 30-MeV, 50-MeV, and 100-MeV neutrons, respectively) as simulated in a Monte Carlo approach [31]. It is worth stressing that these detection characteristics favor considerably the counting of evaporationlike neutrons whose energy is essentially lower than 10 MeV and that the neutrons from the fast INC step are registered with much less efficiency. This feature is central to the method used for estimating E^*.

Figure 4 displays the event yield plotted as function of the amplitude of the associated prompt signal and the neutron multiplicity, measured with a 2-mm-thick Pb target bombarded by the 1.22-GeV antiproton beam (left) or by a 1.22-GeV proton beam (right). The calibration of the light signal has been obtained from the light generated by the charged muons arising from the nuclear reactions induced by the cosmic rays in the atmosphere, the trajectories of the muons being defined along a diameter by two plastic scintillator detectors located on both sides of the BNB.

In Fig. 4 (left), the annihilation events form a broad group associated with large light amplitudes and multiplicities. The corresponding figure for proton-induced reactions at the same bombarding energy [Fig. 4 (right)] is quite different, the event yield being concentrated along a continuous ridge projecting out of the origin, and the most probable light amount is lower by about a factor of 3 compared to the antiproton case. The apparent lack of correlation between the light amplitude and the neutron multiplicity observed in Fig. 4 (left) can be explained as follows: as E^*, or equivalently Mn, increases the number of pions escaping the nucleus decreases (only slightly actually, by 30% between $E^* = 200$ MeV and $E^* = 1$ GeV for U) but their kinetic energy is also reduced. Since the BNB measures only the energy loss of the pions passing through (which represents only roughly 30% of their kinetic energy on an average), and since the energy loss increases with lower kinetic energy, the overall variation of the prompt-signal amplitude with E^* is weak.

LCPs (H and He isotopes), IMFs, fission fragments (FFs) and heavy evaporation residues (HRs) were detected by the BSiB composed of 162 independent silicon detectors (0.5 mm thick, pentagonal and hexagonal in shape) forming a
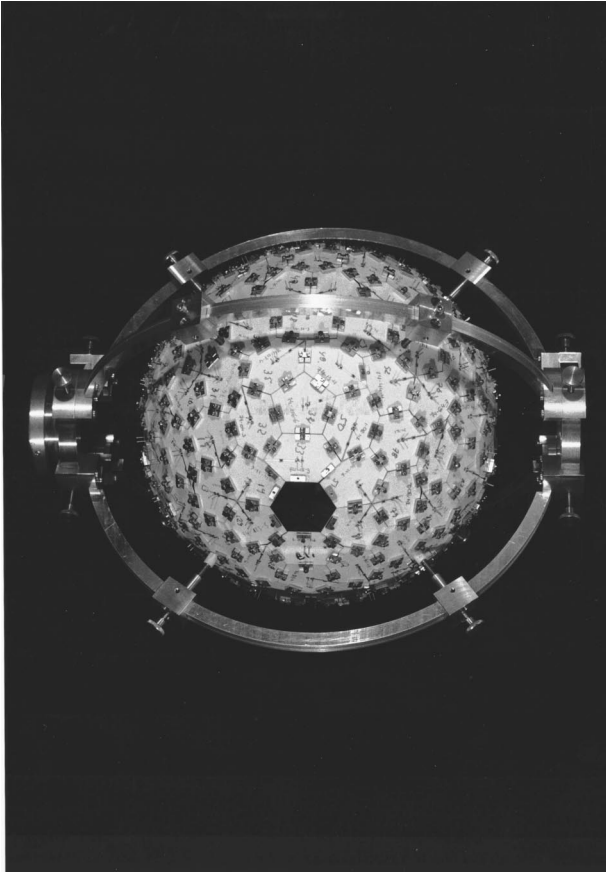
FIG. 5. Photograph of the BSiB in its supporting frame.

FIG. 6. Top: Experimental (circles) and simulated (histograms) angular distributions for p, α particles, and IMFs. The isotropic distributions depicted by the dotted curves were used as inputs for the Monte-Carlo simulations, which took into account the energy loss in the target foil. Bottom: Corresponding detection efficiency curves for the different particles, as deduced form the simulations.

sphere, 20 cm in diameter (Fig. 5). These detectors cover an active solid angle of 90% of 4π sr. Due to the absorption of charged particles in the target foil itself when the particles are emitted at a small relative angle with respect to the latter, Monte Carlo simulations had to be performed in order to infer the actual BSiB efficiency for all types of particles (Fig. 6). The latter amounts to 84%, 81%, and 79% for protons, α-particles, and IMFs, respectively. For FFs, the detection efficiency depends strongly upon the mass and kinetic energy of the fragments, which in turn are related to the depletion in A and Z of the nucleus with increasing E^* in the INC step. Monte Carlo simulations have been performed in order to first infer the characteristics of the fragments issued from the two-step formation process, including the INC step and the deexcitation/fission (using the evaporation computer code GEMINI [28]) and then to take into account the energy loss and straggling in the target foil as a function of the emission angle relative to the target plane [20]. For U, the probability to detect both FFs in coincidence amounts to 0.60 at low E^* and falls to 0.45 at $E^* = 1000$ MeV. The estimated uncertainty in these figures is $\pm 10\%$ as could be checked by measuring under the very same conditions the FFs from a Cf source deposited on a very thin Ni backing. As for the Au target, the fission detection efficiency is further reduced [to 0.50 and 0.30 ($\pm 20\%$), respectively] due to the lower kinetic energy imparted to the fragments resulting from a lower Coulomb repulsion from a less charged nucleus.

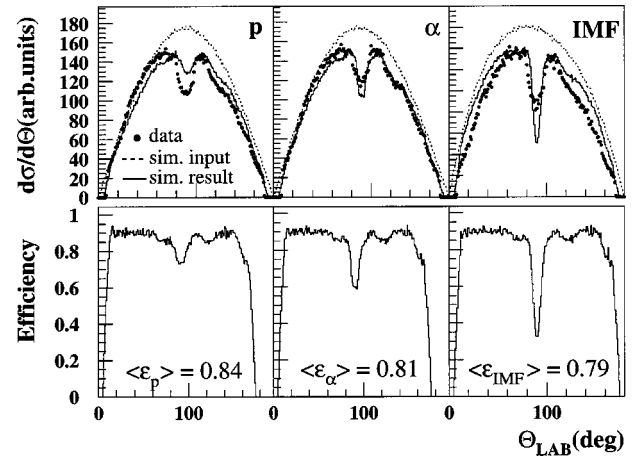Time-of-flight signals, energy signals, and pulse-shape-

discrimination (PSD) signals were generated (one of each per charged particle) and processed by 20 eightfold time-to-digital converters (TDCs), analog-to-digital converters (ADCs), and charge-to-digital converters (QDCs) from SILENA. The electronic threshold was lower than 2 MeV for all detectors. The pulse shape information was obtained from the amplitude of the differentiated current pulse of the preamplifier. The time-of-flight (TOF) information was relative to the START detector with an overall time resolution of about 1 ns.

Different levels of identification are considered. As shown in Fig. 7, the TOF vs E information allows three groups of data points to be distinguished, corresponding to the heaviest nuclei (FFs and HRs), to IMFs, and to LCPs. The distinction between $Z=1$, $Z=2$, and IMF makes use of the E vs PSD signals as shown in Fig. 7. Protons and alpha particles of energy larger than 8.2 and 32.2 MeV, respectively, are not stopped in the 0.5-mm-thick Si detectors but α particles with energies up to about 55 MeV can nevertheless be identified. Isotopic separation of $Z=1$, 2 particles has not been considered since it is only possible in a restricted energy domain. The distinction between IMFs and α particles is unambiguous above 25 MeV from the E vs PSD matrix, and still
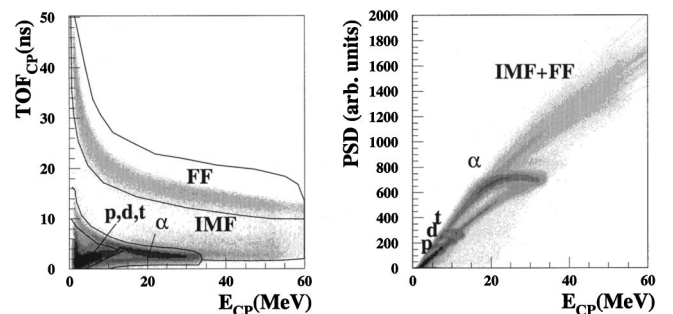

FIG. 7. Identification matrices for the BSiB detectors: energy vs time of flight (left) and energy vs pulse-shape discrimination parameter.

possible below this energy from the TOF vs E information.

For heavier fragments a mass calibration has been performed from TOF vs E information, considering usual instrumental effects such as pulse-height defects [32] and plasma-delay effects [33,34] in Si detectors. Use has been made of rather cold-fission events (associated with low neutron multiplicities) for the U target in order to further adjust the calibration parameters. It has been checked for different classes of events (at different excitation energies) that the summed mass of all light- and intermediate-mass particles (after proper detection efficiency corrections) and both fission fragments led on the average to a mass fairly close to the target mass. As a matter of fact some deficit was generally observed, as due to the mass of high-energy particles (both LCPs and neutrons) from the INC step that are not detected. The mass resolution of the FF is estimated to be of the order of 10–20 %, arising from the limited flight path of 10 cm and TOF resolution. Fission events were selected as binary events with two fragments heavier than a certain imposed mass threshold (30 and 35 mass units for the Au and U targets, respectively), to be distinguished from IMFs, with the additional condition that 70% of the initial mass is detected.

The HRs suffer more than any other reaction product from the slowing down in the target. Due to the low recoil momentum imparted in the INC stage, their extraction from the target is greatly facilitated by the subsequent recoils accompanying the evaporations of light particles p or n and more efficient, the emissions of α particles and IMFs, as demonstrated in Sec. V C. They are thus detected with a larger probability at higher excitation energy: ϵ_{HR} is estimated at only 0.06 ($\pm 30\%$) at $E^* = 200$ MeV, but increases to 0.35 ($\pm 20\%$) at $E^* = 200$ MeV. Alternatively, the HRs have also been experimentally selected in the events for which the total measured mass represents more than 70% of the target mass with only one detected fragment with a mass larger than the minimum one attributed to a FF, as defined above, for the considered target. The conditions of the HR detection being rather difficult to control, one relies also on the high detection probability of at least one of the two FF fragments in order to infer their emission probability. Indeed in events for which the greatest detected mass is an IMF, the probability of missing both fission fragments can be computed, with the complementary part attributed to HRs.

The master trigger of the acquisition system was a coincidence between the signal of the START scintillator, non-vetoed by the annular detector, and the prompt light signal of the BNB, with a threshold of about 10 MeVee, as calibrated with the cosmic muons.

IV. DATA RELATED TO EXCITATION ENERGY DEPOSITION

The present investigation considers all decay channels with a ''genuine'' minimum-bias trigger in so far as the total reaction cross section is probed. It does not focus on selected and rare exit channels. Instead, one has tried to get a comprehensive picture of *all* phenomena that are at work as a
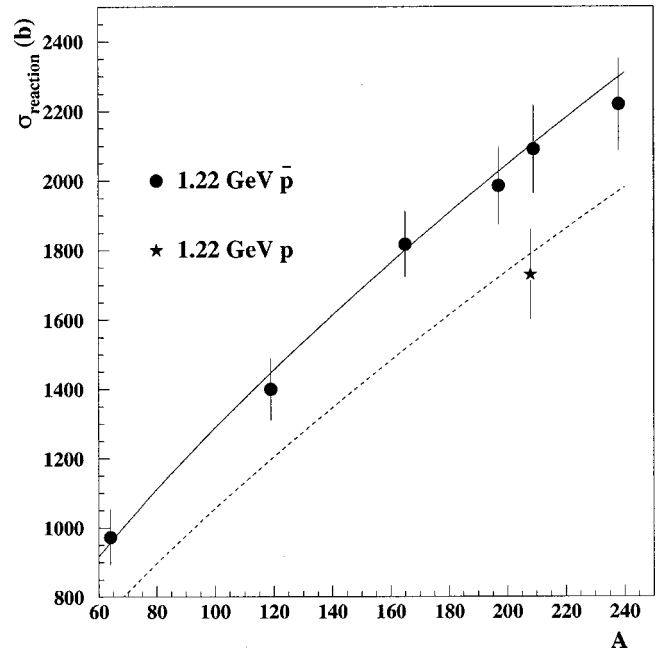

FIG. 8. Total reaction cross sections measured in this work plotted as a function of the target mass (dots). The solid curve corresponds to a fit with the function $\sigma_{\text{reaction}} = \pi r_0^2 A^{2/3}$, $r_0 = 1.38$ fm. The dashed curve corresponds to the systematics of Ref. [35] for p-induced reactions and the star to the experimental result of Ref. [36], obtained with the same technique as the present work.

function of the excitation energy that is deposited in the struck nucleus by the incident $\bar{p}$.

A. Reaction cross sections

The high sensitivity of the scintillator detector to any kind of emitted particle makes it particularly suited to register all inelastic reaction channels. The $\bar{p}$-nucleus reaction cross sections (for events associated with a prompt response greater than 10 MeV) are shown in Fig. 8 together with the p-nucleus cross sections systematics [35] (dashed curve), as a function of target mass A. Both distributions can be well fitted with a function of the form $\pi r_0^2 A^{2/3}$, with $r_0 = 1.38$ fm for the antiprotons (solid curve in Fig. 8) and 1.26 fm for the protons. The larger r_0 radius of the disk needed to fit the $\bar{p}$ nucleus relative to the p-nucleus cross sections can be interpreted as the consequence of larger elementary $N\bar{N}$ cross sections in the former case. Also, the strong dependency on energy of the $N\bar{N}$ cross sections can be stressed when comparing the present data with those obtained at a lower bombarding energy [37].

B. Correlated neutron and charged-particle multiplicities for a series of targets: ^{12}C, ^{nat}Cu, ^{89}Y, ^{92}Mo, ^{100}Mo, ^{nat}Ag, ^{nat}Sn, ^{165}Ho, ^{197}Au, ^{209}Bi, and ^{238}U

The correlated neutron and light charged particle multiplicities are presented in Fig. 9. They have been measured for a series of targets from C to U and for an empty target frame. This spurious contribution is easily removed from all measurements and does not impair the quality of the data.
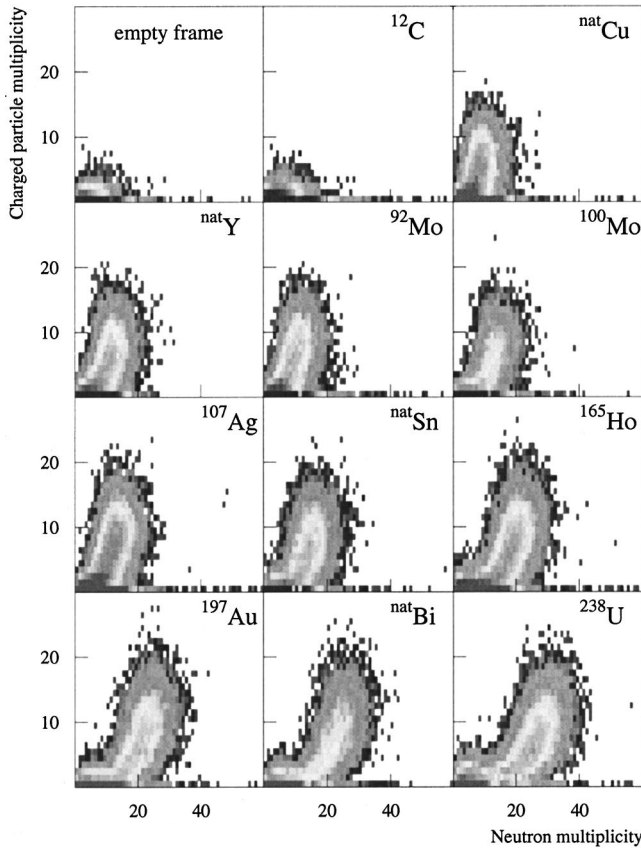
FIG. 9. Experimenal yield of 1.22-GeV $\bar{p}$-induced reactions plotted as a function of the measured neutron and charged-particle multiplicities for different targets and an empty frame. No background was subtracted.

Similar patterns have already been observed [38] in heavy-ion induced reactions. When starting from the origin of the distribution (very weakly excited nuclei with neither a single neutron nor a single light particle detected but nevertheless a trigger provided by γ rays or charged pions) one observes a continuous evolution, with a pattern strongly depending upon the nature of the targets. For light targets there is no offset for charged-particle emission in contrast to what is observed for heavy targets. This reflects Coulomb barrier effects: at low excitation energy a heavy nucleus evaporates neutrons much more easily than charged particles whereas at high excitation energy this Coulomb hindrance becomes less effective. This Coulomb effect is much weaker for light target nuclei, as evidenced by the observation of a more balanced sharing between neutron emission and charged-particle emission at all excitation energies. The excess of neutrons observed for the ^{100}Mo target as compared to ^{92}Mo target can be ascribed to the difference in the neutron-separation energies. All these plots indicate that the measured particles are mostly evaporated ones as expected from the energy-dependent efficiencies of the detectors. This is confirmed in Fig. 10 displaying contour plots of the invariant velocity distributions of LCPs, detected for the Au target—their angular isotropy manifests the dominant evaporative character. It has been checked that this isotropic character of the angular distributions is maintained independent of the
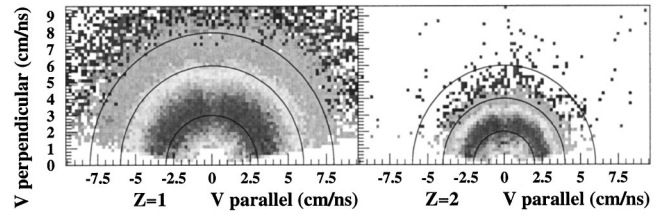

FIG. 10. Galilei-invariant velocity distributions measured for $Z=1$ and $Z=2$ particles, plotted as a function of the velocities parallel and perpendicular to the beam. The circles, displayed for orientation, are centered on the origin.

associated total light-particle multiplicity.

The measured neutron multiplicity (M_n) distributions, corrected for the correlated and noncorrelated backgrounds, are shown in Fig. 11. In the tails of the distributions and for the lighter targets (C and to a lesser extent Al) the neutron number is found to exceed the number of neutrons contained in the target nucleus. Such an effect is not related to pile-up effects but to secondary reactions induced by the escaped pions either in the liquid scintillator or in the BNB walls, thus generating extra neutrons. The average multiplicity of these neutrons has been estimated to 1.9 for the Au target from Monte Carlo simulations with the high-energy computer code GEANT [39].

Coming back to Fig. 11, it can be noted that the multiplicities of about 30–35 neutrons observed for the Au and Pb target nuclei represent about one-half of the neutron multiplicity observed [40] with a similar probability when a 29-
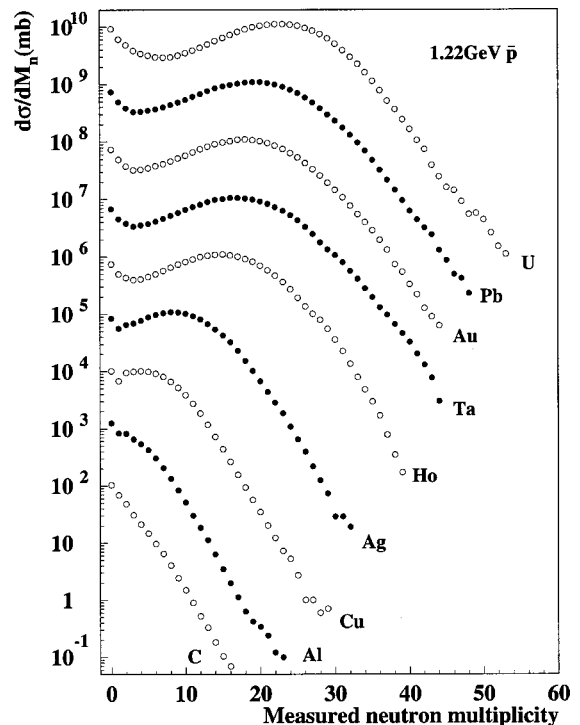

FIG. 11. Experimental inclusive neutron multiplicity distributions for different targets, corrected for correlated and uncorrelated backgrounds. The distributions are multiplied by successive factors of 10 for clarity, from C onward.
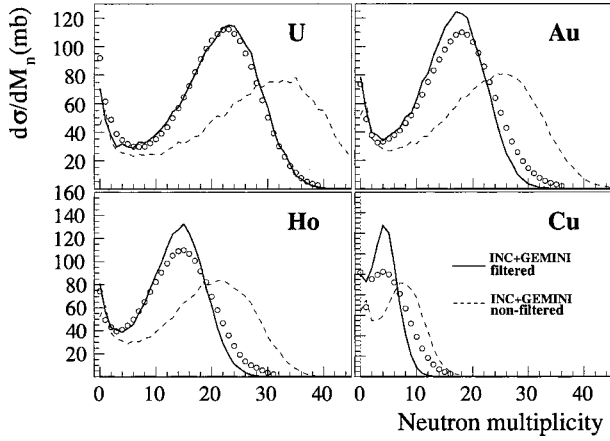
FIG. 12. Comparison between the measured (circles) and theoretical (curves) neutron-multiplicity distributions for different targets. The dashed curves depict the true distributions calculated with the combined models INC+GEMINI, while the solid curves correspond to the distributions filtered with the BNB efficiency.

MeV/nucleon Pb projectile collides with a Au target. This readily demonstrates that heating a nucleus with an antiproton can be roughly as effective as in a nucleus-nucleus collision induced at intermediate bombarding energy with similar available energy (3 GeV). However the decay patterns of nuclei heated to similar energies are comparable at low excitation energies only, where fission and evaporation leading to residues dominate in both cases. At high excitation energy, the Pb+Au system disintegrates [40] into a large number of nucleons and small fragments, whereas binary fission and evaporation remain by far the dominant exit channels of the Au nucleus initially heated by antiprotons. As already stressed, the fates of nuclei at high excitation energy can be strongly influenced by the collective excitations and the strong dynamical effects experienced in nucleus-nucleus collisions.

The neutron distribution has first been corrected for background and for the spurious neutron production in the scintillator. With the neutron detection efficiency depending on the neutron energy, it is easier to fold the results of the calculation with the detector efficiency and compare them with the raw experimental data. This is done in Fig. 12 where the dashed lines represent the true neutron multiplicity distribution as generated in both the INC and evaporation stages of the simulation. Because of the very rapid loss of efficiency for neutrons exceeding 20 MeV, the efficiency-folded, simulated data (solid lines in Fig. 12) mostly retain the low-energy, evaporated neutrons. A good agreement with the experimental data, both in shape of the distributions and absolute cross sections is found for the heaviest targets (Ho, Au, U). For Cu and the lightest target nuclei in general, the agreement is poorer. This effect is attributed to the relative weight of spurious neutrons created in the scintillator liquid, which increases as the target mass decreases. This experimental problem is specific to neutrons and does not blur the charged-particle data. The average experimental neutron multiplicity data corrected for background and spurious pion production are listed in Table I. The given error bars stem

TABLE I. Average measured neutron multiplicities $\langle M_n \rangle$, average neutron multiplicities corrected for the BNB efficiency and the electronic dead time $\langle M_n \rangle^{corr}$ for different target nuclei using 1.22-GeV $\bar{p}$ or $\bar{p}$ at rest. For 1.22-GeV $\bar{p}$, the efficiency-corrected, average multiplicities measured [41] with a time-of-flight spectrometer are given for comparison.

$_Z^A X$	$\langle M_n \rangle$	$\langle M_n \rangle^{corr}$	$\langle M_n \rangle^{TOF}$
		1.22-GeV $\bar{p}$	
^{12}C	1.6±0.2	1.9±0.5	
^{27}Al	2.6±0.3	5.1±0.5	
^{nat}Cu	5.0±0.6	8.8±1.5	8.9
^{nat}Ag	8.0±1.0	13.1±2.0	12.9
^{165}Ho	12.8±1.5	19.6±3.0	20.8
^{181}Ta	14.7±2.0	22.2±3.5	22.4
^{197}Au	15.4±2.0	23.2±4.0	23.4
^{nat}Pb	16.3±2.0	24.4±4.0	22.9
^{238}U	18.2±2.0	26.5±4.5	27.5
		$\bar{p}$ at rest	
^{nat}Cu	1.7±0.2	1.9±0.4	
^{165}Ho	6.8±1.4	8.2±1.6	
^{197}Au	7.4±0.9	8.9±1.8	
^{238}U	9.6±1.1	11.7±2.3	

mostly from the correction uncertainties and very little from statistics. It is noticeable that the observed multiplicities exceed considerably the ones measured from annihilation of antiprotons at rest measured in the same experiment, also given in Table I. This increase results from the larger available energy and is linked to the Lorentz boost imparted to the pions, providing them with larger average kinetic energy (450 MeV instead of 250 MeV) and forcing them to interact more intimately with the target nucleus.

Charged-particle multiplicity data are shown globally and for different Z numbers in Fig. 13 and Table II. The IMFs contribute rather weakly in comparison to $Z=1, 2$ particles to the total charged-particle multiplicity. This is the first hint that multifragmentation must be weak in such reactions, if contributing at all for heavy targets.

The excitation energy E^* has been reconstructed on an event-by-event basis. The method [18] used for this reconstruction makes use of the total measured light-particle (LP) multiplicity, which minimizes the fluctuations arising from the stochastic nature of the decay and associates with it E^*. From the experiment it is not possible to distinguish on an event-by-event basis the number of evaporationlike neutrons, i.e., the ones that account for the cooling of the thermalized nucleus from those emitted before thermal equilibrium is achieved, thereafter referred to as cascade neutrons. Monte Carlo simulations have shown that the detected cascade neutrons compensate to a large extent for the nondetected evaporated ones, on average. To reconstruct E^*, it has thus been assumed [18] that the measured neutron multiplicity can be identified with the multiplicity of evaporated neutrons. The correctness of this method has been tested on an average, thanks to a separate experiment [41] measuring the inclusive neutron kinetic-energy distributions for the same reactions.
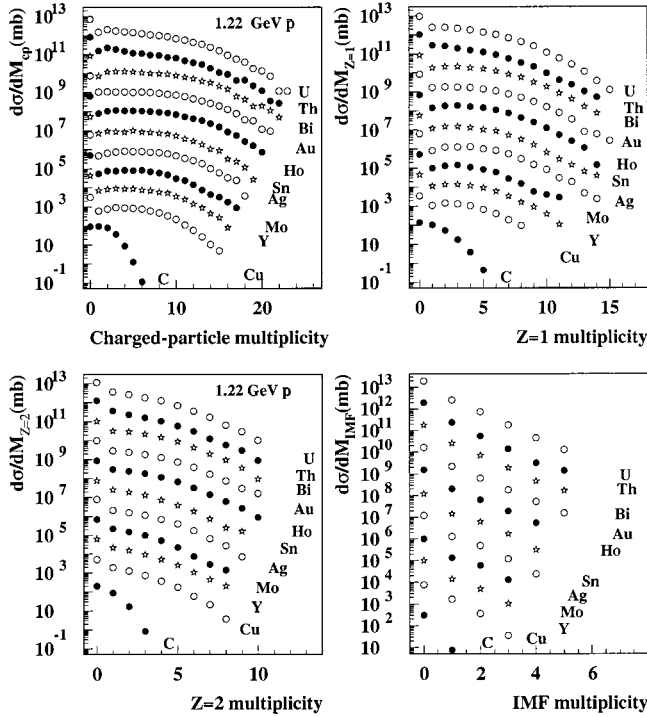
FIG. 13. Experimental distributions (symbols) of multiplicities of total light particles, $Z=1$, $Z=2$ and IMFs, for different targets (multiplied by successive factors of 10 for clarity).

Once folded with the BNB efficiency, these spectra have enabled the equivalent neutron multiplicity as measured by the BNB to be computed, and it has been checked that the latter reflects closely that of the evaporative component identified in these spectra. The relation $M_{LP}(E^*)$ was calculated with GEMINI (see Fig. 1). In Fig. 14, the experimental yield for Au is plotted in a contour diagram as a function of the so-obtained E^* and M_n (a) or M_{LCP} (b). The model predictions for the average multiplicities folded with the detection response (dots connected by a line) fit closely the ridge of the distributions, showing that the sharing between n and LCP is well accounted for by the model on average. This good reproduction gives support to the validity of the E^*-assessment method.

TABLE II. Average inclusive multiplicities of light-charged particles, corrected for the BSiB efficiency, for the different target nuclei.

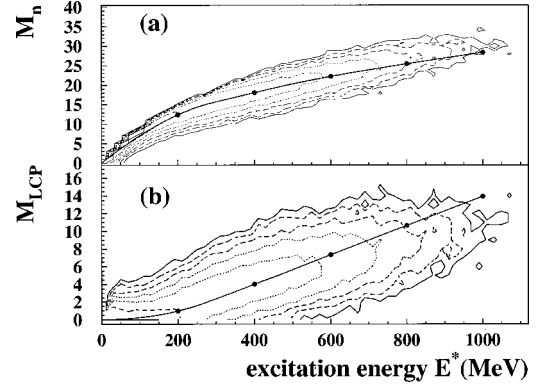| $_Z^A X$	$\langle M_{CP} \rangle$	$\langle M_{Z=1} \rangle$	$\langle M_{Z=2} \rangle$	$\langle M_{IMF} \rangle$
^{12}C	1.5 ± 0.2	1.0 ± 0.1	0.5 ± 0.1	0.04 ± 0.10
^{nat}Cu	3.8 ± 0.5	2.4 ± 0.3	1.2 ± 0.2	0.33 ± 0.10
^{89}Y	4.0 ± 0.5	2.4 ± 0.3	1.2 ± 0.2	0.31 ± 0.10
^{92}Mo	4.1 ± 0.5	2.4 ± 0.3	1.2 ± 0.2	0.30 ± 0.10
^{nat}Ag	4.2 ± 0.5	2.6 ± 0.3	1.3 ± 0.2	0.27 ± 0.10
^{nat}Sn	4.5 ± 0.6	2.7 ± 0.4	1.4 ± 0.2	0.30 ± 0.10
^{165}Ho	4.8 ± 0.6	2.8 ± 0.4	1.6 ± 0.3	0.31 ± 0.10
^{197}Au	4.9 ± 0.6	2.8 ± 0.4	1.6 ± 0.3	0.29 ± 0.10
^{209}Bi	4.8 ± 0.6	2.9 ± 0.4	1.7 ± 0.3	0.28 ± 0.10
^{238}U	4.8 ± 0.6	2.8 ± 0.4	1.6 ± 0.3	0.26 ± 0.10

FIG. 14. Contour diagrams of experimental yield as a function of E^* and M_n (upper panel) or M_{LCP} (lower panel), compared with calculated average multiplicities (dots connected by a line). The intensity change between two contour lines is a factor of 3.

At $E^* \simeq 1$ GeV, once corrected for efficiency, the present average experimental LCP multiplicity amounts to about 12 units. This value is in good agreement with those extracted in previous works [42,43] on heavy-ion induced reactions for a similar E^*.

The experimental E^* distribution can be compared with the one generated by the INC model. The result, shown in Fig. 15, is satisfactory over a broad range of excitation energies for target nuclei of different masses. For target nuclei with masses close to 200 (from Ho to U), excitation energies of up to 1 GeV are reached, i.e., roughly 5 MeV/nucleon. They nevertheless represent rather rare events and thus small
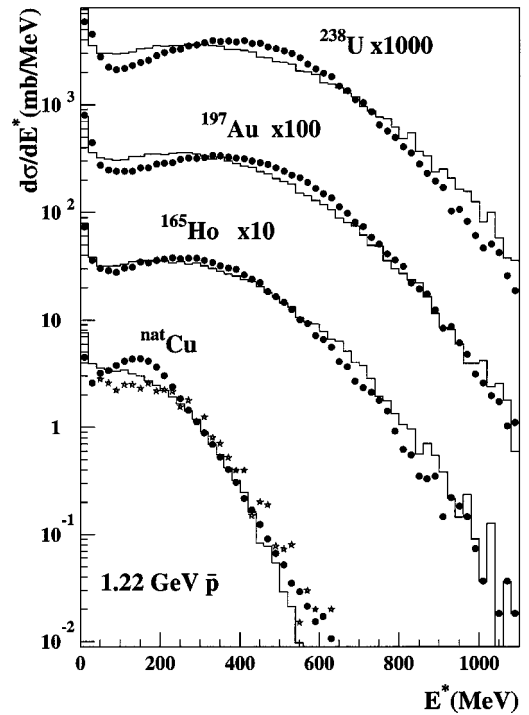

FIG. 15. Experimental (circles) and theoretical (lines) excitation energy distributions for 1.22-GeV $\bar{p}$ reactions induced on different target nuclei. For Cu, the stars show the E^* distribution constructed from the measured LCPs only.

TABLE III. Average excitation energies $\langle E^* \rangle$ deduced with the method described in the text, estimated average excitation energies per nucleon using the masses predicted by the INC model, $\langle E^*/A \rangle$ (in parentheses, maximum excitation energies per nucleon corresponding to 1% of the reaction cross section) for different target nuclei, obtained with 1.22-GeV $\bar{p}$ or $\bar{p}$ at rest. The corresponding energies $\langle E^*_{\text{INC}} \rangle$ and $\langle E^*_{\text{INC}}/A \rangle$ predicted by the INC model are given for comparison, as well as the average energies measured by Polster *et al.* [22] with $\bar{p}$ at rest $\langle E^*_p \rangle$.

$^A_Z X$	$\langle E^* \rangle$ (MeV)	$\langle E^*/A \rangle$ (E^*_{max}/A) (MeV/A)	$\langle E^*_{\text{INC}} \rangle$ (MeV)	$\langle E^*_{\text{INC}}/A \rangle$ (MeV)	$\langle E^*_p \rangle$ [22] (MeV)
		1.22 GeV-$\bar{p}$			
^{nat}Cu	144±20	2.53 (11.3)	135	2.5	
^{165}Ho	269±30	1.73 (5.4)	265	1.7	
^{197}Au	309±30	1.65 (5.4)	295	1.6	
^{238}U	348±40	1.52 (4.3)	330	1.5	
		$\bar{p}$ at rest			
^{nat}Cu	85±20	1.44 (5.7)	87	1.52	130±15
^{165}Ho	138±30	0.88 (3.3)	145	0.93	187±26
^{197}Au	142±30	0.74 (2.7)	158	0.83	183±21
^{238}U	161±40	0.70 (2.3)	171	0.75	160±20

cross sections (a few millibarn). Although a more effective heating mode than antiprotons at rest (the average E^*, listed in Table III, are about twice as large) or than protons at the same bombarding energy, the 1.22 GeV antiprotons remain a modest heat converter, since at the very best one-third of the available energy of 3.1 GeV (kinetic+annihilation energy) can be found in excitation energy and moreover just with a tiny fraction of the reaction cross section. This is somewhat less effective than the use of medium-energy heavy-ion projectiles as heaters and this represents a ''price to pay'' in order to avoid the collective excitations inherent in the latter type of projectiles. For lighter target nuclei such as Cu the energy deposition, although weaker than in heavy targets, reaches values of up to 10 MeV/nucleon, which exceed the binding energy. The fate of light nuclei, more effectively heated than heavy ones, is the topic of another paper [21].

C. Discussion of the merits of different projectiles

In the light of what precedes, it is worthwhile to review the arguments determining the choice of a projectile for studies devoted to the thermal decay properties of nuclei. Must the projectile be a composite particle, a single baryon, a meson, or an antiparticle?

Composite particles such as ^{3}He have been shown to present some of the drawbacks of more massive nuclei although to a lesser extent [44]. Moreover, it has been shown [45] that by using ^{3}He or a proton as a projectile, both with a total kinetic energy of 2 GeV, leads to rather similar excitation energies in massive target nuclei, thus giving no decisive advantage to the heavier projectile with respect to energy dissipation. Similar mass yield curves found [46] for protons and heavy-ions at the same total kinetic energy is indicative of the same effect. For these two reasons there is

thus no obvious motivation for using composite particles as projectiles, since they already bring in part of the drawbacks of more massive ones.

There is no decisive advantage either in choosing a meson rather than a baryon as a projectile for heating a nucleus. The nuclear stopping of pions has been shown to be very similar to that of protons with the same energy over a broad energy domain [47,48]. A less direct approach [49,50] has confirmed this property: positive and negative pions, positive kaons, protons (and even deuterons) of a given energy generate very similar numbers of neutrons by spallation on thick targets. It was also shown [49,50] that antiprotons and protons had a similar behavior in so far as the total available energy was considered (i.e., taking the annihilation energy in addition to the kinetic energy for the antiparticle) for producing neutrons in thick targets. A similar conclusion has been obtained [51] from the study of the fragment mass distributions using radiochemical techniques. A recent experiment with protons on thin targets (more relevant than the experiments implying thick targets in so far the energy deposition in a given nucleus is concerned) shows large similarities in energy deposition for a 2.5-GeV proton and the presently studied 1.22-GeV antiproton, i.e., for two hadrons with close total energies [52]. The merits of antiprotons, protons, and π-mesons for heating a nucleus have also been investigated in a recent experiment [14] and at higher bombarding energies showing slightly larger E^* with the former projectiles. Although antiproton annihilation carries no decisive advantage over protons or pions as for the E^* generation, it is possible as suggested in Ref. [53] that it involves a lower mass loss in the INC stage and that thermal equilibrium is reached faster. A careful comparison of the decay of the nuclei excited via these different processes would be very enlightening in this respect. In principle, the recent 2.5-GeV-proton experiment mentioned above will enable such a comparison, under very similar experimental conditions. The best possible choice could actually be a beam of $\bar{d}$, which may be available in the near future, at a quite moderate bombarding energy around 1.5 GeV/nucleon in order to still benefit from the softness of this heating mode.

V. DECAY PROCESSES

A. Fission

Before presenting the experimental fission data, some theoretical predictions for fission from the combined INC +statistical models will be given for orientation. For the statistical model (SM), the code GEMINI has been used, but the code ABLA [54] has also been applied to demonstrate that though the quantitative aspects may vary, the gross features are largely independent of the specific models employed. It must be recalled that the SM does not consider any dynamics and that, while a transient delay for the motion from equilibrium to the saddle point has been introduced in both codes, the shape evolution from the saddle to the scission points is not taken into account. Consequently, the evaporation from the composite nucleus is immediately followed by that from the separated fragments. In the following, only mass-symmetric fission is considered.

1. Theoretical properties of the fission events

The population of primary nuclei from the INC stage that will eventually undergo fission will be considered first. One may expect that these nuclei are proton richer than those eventually ending up as evaporation residues. The loss of more neutrons and/or fewer protons than average during the INC stage leads to an enhanced fissility Z^2/A of the resulting primary nuclei and thus to a reduction of the associated fission barriers. This expectation is supported by the calculation as illustrated in Fig. 16 displaying the fission probability for $\bar{p}+$Au and $\bar{p}+$U as a function of the N and Z numbers of the nuclei as they are left at the end of the INC step (the nuclei with $Z>Z_{\text{target}}$ or $N>N_{\text{target}}$ are produced in charge exchange reactions). For orientation, the yield of the latter is plotted in a linear scale as contour lines. The fission probability is much higher for nuclei with N and Z close to those of the target nucleus (associated with low E^*) in the case of U as compared to Au, as expected from the difference in fissility. However, in both cases, only proton-rich primary nuclei undergo fission with a sizable probability.

The time scales characterizing the fission process are of prime interest since they provide unique information on the dynamics. For the primary nuclei produced with the Au target, the fission barriers are fairly high ($B_f \simeq 20$ MeV); consequently, the fission must occur before too much energy is lost via the evaporation of light particles. This problem is less severe for the primary nuclei produced from U target nuclei, associated with fission barriers as low as 6 MeV. A larger number of presaddle particles is thus allowed in the latter case. This behavior is illustrated in Fig. 17 where the numbers of presaddle particles are compared to the total numbers of evaporated particles as a function of E^*, for the Au and U targets: the average multiplicities of presaddle protons and α particles are about twice as large and that of neutrons three times as large for U as for Au. All presaddle multiplicities remain roughly constant for E^* larger than 300 MeV, which means that the fraction of the post-saddle particles (considered as emitted by the FFs in the calculation, as already pointed out) increases continuously with E^*. By summing up the times elapsed between the evaporation of two consecutive presaddle particles, as deduced from the total widths, the fission presaddle time can be estimated. The so-obtained average presaddle times are plotted in Fig. 18 as a function of the excitation energy of the primary nuclei. As expected, the different multiplicities of presaddle particles for the Au and U cases translate into different presaddle time scales, the difference reaching a factor of 10 or more for $E^*>300$ MeV. For Au, the predicted fission time at high E^* becomes of the same magnitude as the thermalization time, estimated at 10^{-22} s (30 fm/c) as mentioned above. Also for $E^*>500$ MeV, the excited-nucleus lifetime, as given by the emission time for the first neutron, becomes shorter than the thermalization time. Both features may cast some doubts on the applicability of the sequential statistical model at high E^*.

2. Fission cross sections

The first data that are presented concern the angle-integrated, total (E^*-integrated) fission cross sections. The
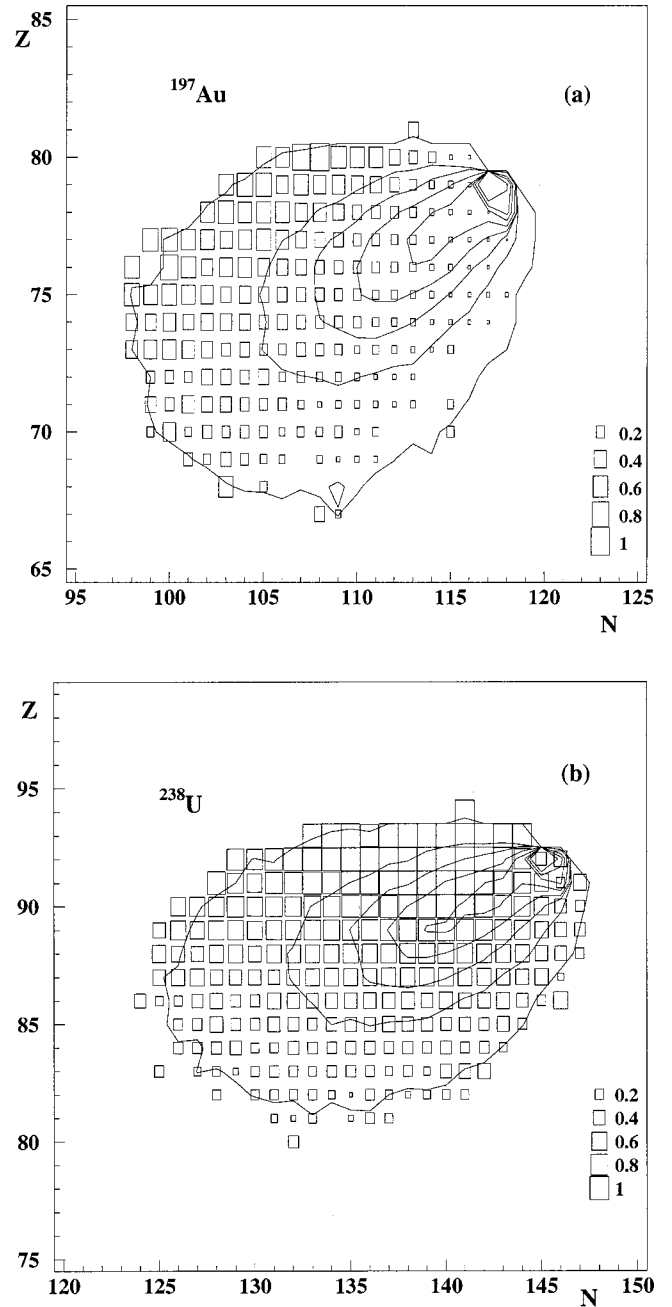

FIG. 16. Fission probability (boxes) plotted as a function of the N and Z numbers of the primary nuclei as calculated by the INC +GEMINI models for the Au and U targets. The contour lines depict the yield in a linear scale with 200 counts between neighboring lines.

fission cross sections amount to 185 ± 81 mb and 940 ± 200 mb for the Au and U targets respectively. Clearly these cross sections increase with the target fissility, as expected for conventional fission. It is interesting to compare these cross sections with those previously measured in proton- or α-induced reactions in the GeV bombarding-energy range [55–57]. For 3-GeV protons, associated with an excitation-energy range probably comparable to that for 1.22-GeV $\bar{p}$, the latter cross sections were found as 103 ± 21 mb [55] or 100 mb [56] for Au and 1210 ± 180 mb [55] or 1321 ± 100
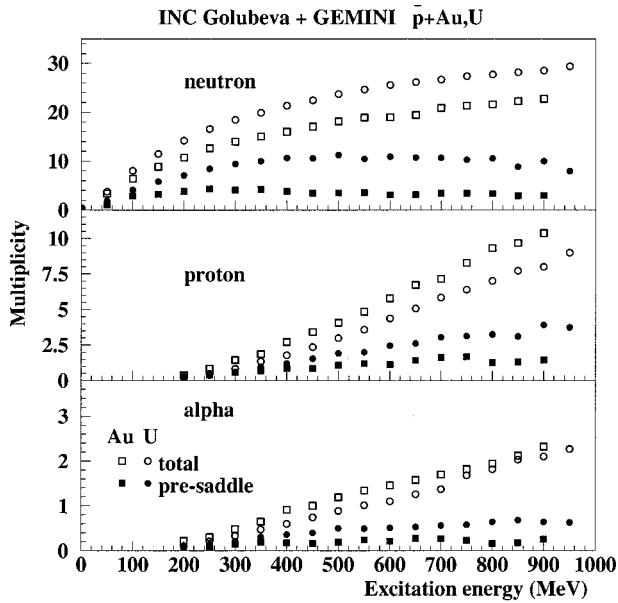
FIG. 17. Theoretical total (open symbols) and presaddle (solid symbols) multiplicities of evaporated particles plotted as a function of the initial excitation energy for the Au and U targets.

mb [57] for U. These cross sections are compatible with those of the present work within the error bars, although they appear slightly lower for Au and greater for U. These possible differences, in addition to resulting from different mass losses in the INC cascade, can be tentatively ascribed to differences in the excitation energy distributions, the fission probabilities at high E^* exhibiting opposite trends as a function of E^* for Au and U as will be shown in the next section. A more detailed comparison with earlier data was made in a previous paper [19]. Slightly different integrated cross sections in [19] (160 ± 11 mb and 920 ± 200 mb for the Au and U targets, respectively) are due to different conditions applied to select the fission events.
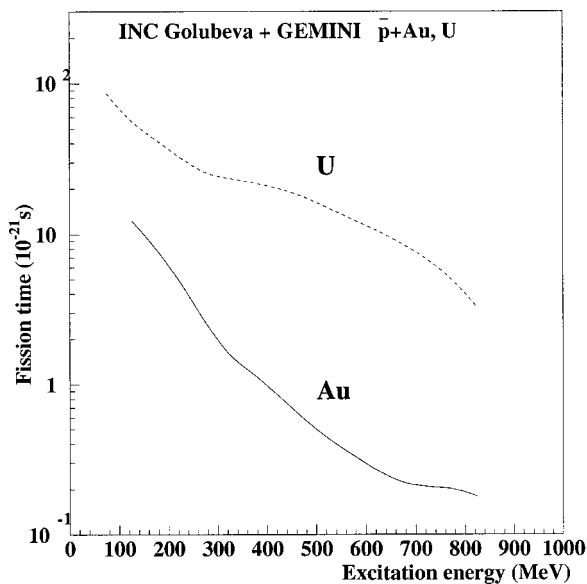

FIG. 18. Theoretical average time for the decision to fission plotted as a function of the initial excitation energy.

No particular effort has been made to reproduce these integrated cross sections theoretically since the evolution of the fission probability as a function of E^*, addressed in the next section, offers a much more stringent test to the theoretical models.

3. Fission probability: Evolution with E^*

The fission probability (P_{fis}) is a key observable for several reasons. On the one hand, the disappearance of fission with increasing excitation energy may manifest the onset of another, less collective breakup channel. On the other hand, the fission probability at high excitation energy is sensitive to the transient time necessary for the fission mode to attain its stationary decay width. The increased presaddle emission of charged particles taking place during this transient time leads to a decrease in fissility, manifesting itself by a reduction of P_{fis}. This effect is all the more prominent at high E^* as the mean evaporation time of light particles decreases. Studying P_{fis} at high E^* is thus a unique means to gain insight into the fission dynamics prior to the saddle point. For instance, other methods involving the measurement of precision neutrons [15] or γ rays [58], or the blocking technique in a single crystal [16], provide only information about the prescission time (pre- + post-saddle time). The sensitivity of P_{fis} to the transient time has already been exploited in several works, in particular by Moretto *et al.* [17] in α-induced fusion reactions, associated with $E^* < 100$ MeV. The latter authors could set an upper limit for the transient time of 3×10^{-20} s. The present experiment allows P_{fis} to be investigated over a considerably broader excitation energy range, enabling significantly shorter time scales to be probed. This question was also discussed for fission following stopped-antiproton annihilation [59–61].

The fission probability has been obtained by dividing the yield at a given E^* of binary-fission events, corrected for the detection efficiency via the procedure described above and detailed in Ref. [20], by the total yield of events associated with that E^*. It must be stressed that the unique features afforded by antiproton annihilation combined with the experimental method employed in this work, set up the proper framework for an investigation of P_{fis} as a function of E^*, the following conditions being met simultaneously, as mentioned above.

(i) The number of nucleons expelled during the INC stage of the reactions being quite moderate (10% of A_{target} at $E^* = 1$ GeV), a well-defined, fairly fissile group of nuclei remains after this stage has subsided. As the fission width drastically depends on the primary nucleus, this feature is central to the present study.

(ii) Since the total reaction cross section is probed, the total yield of events at a given E^* can be determined.

(iii) E^* is assessed via a procedure based on the total number of evaporated light particles, and is thus highly independent of the decay channel, i.e., of whether the nucleus undergoes fission or not.

The fission probabilities measured for $\bar{p}$ + Au and U are shown in Fig. 19 as a function of E^*. Since at high E^* the mass distribution of the fission fragments (FF) broadens con-
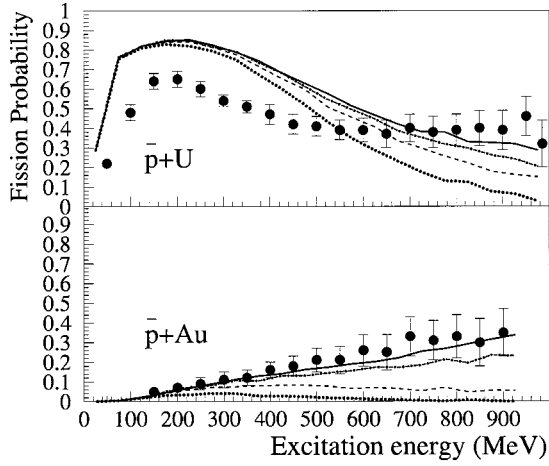
FIG. 19. Experimental fission probability (solid points) plotted as a function of the initial excitation energy of primary nuclei formed in $\bar{p}$ + Au and U. The curves correspond to theoretical results obtained with INC+GEMINI for different transient times τ_f: $\tau_f = 0$ (solid), 0.1×10^{-21} s (dot-dashed), 0.5×10^{-21} s (dashed), 2×10^{-21} s (dotted).

siderably, the distinction between a FF and an IMF becomes somewhat ambiguous. Consequently different mass cuts have been applied [20] to the data, the error bars in Fig. 19 depicting the effect of a ± 10-unit change in the cut. The behaviors of P_{fis} for the two targets are very different: for the Au target P_{fis} steadily increases with increasing E^*, whereas it first rises steeply and then slowly falls off for U. This observation strongly suggests that the fissility remains the driving parameter and that conventional fission, and not a mechanical process, as advocated in Ref. [62], for example, is present here.

A very important conclusion can be readily drawn from Fig. 19: fission remains a very substantial decay channel at $E^*/A > 4$ MeV/nucleon, exhausting more than a third of the yield. This finding has two major implications. (i) The nucleus appears to keep conventional properties up to the above excitation energy; and (ii) this significant abundance of fission points to a quite short transient time needed to reach the saddle point at such high excitation energies.

The latter conclusion arises from the expectation that a large transient time would lead to a dramatic reduction of P_{fis} at high E^* as both the remaining E^* and the fissility would have dropped considerably by the time the saddle point is reached.

The set of curves in Fig. 19 represent the results of the INC+GEMINI calculations for different values assumed for the transient time τ_f, varying from 0 to 2×10^{-21} s. The a_f/a_n ratio has been taken as 1.022 and 1.00 for Au and U, respectively, in agreement with the expected tendency and with the ratios used previously in similar works [63]. The general trend is correctly reproduced by the calculations assuming no transient time for the two targets, although P_{fis} is overestimated at low E^* for the U case. The inclusion of a delay larger than $\tau_f = 0.5 \times 10^{-21}$ s leads to a strong deterioration of the quality of the agreement at high E^*. It is important to note that the ratio a_f/a_n and the transient time, as

implemented in GEMINI, do not affect the dependence of P_{fis} on E^* in similar ways: while a_f/a_n governs the magnitude of P_{fis} over the full E^* range, τ_f rules P_{fis} only at high E^*. The two parameters can thus be determined independently via $P_{\text{fis}}(E^*)$, while their respective influences cannot be disentangled from the integrated fission cross sections alone. This conclusion will actually be qualified when employing the model ABLA instead of GEMINI.

The limit on the transient time can be reasonably set to 1×10^{-21} s, more than an order of magnitude lower than established in the work of Moretto *et al.* [17].

4. Comparison with the predictions of ABLA

In order to test the previous conclusions obtained with GEMINI, further comparisons have been made with ABLA [54]. ABLA computes the fission probability with the transition-state formalism [64] of Bohr and Wheeler (BW) as GEMINI does, but the fission hindrance related to the viscosity is taken into account as proposed in Ref. [65] via a reduced viscosity parameter β. The fission probability P_{fis} is deduced from the fission width Γ_f and the neutron emission width Γ_ν as follows:

$$P_{\text{fis}} = \frac{\Gamma_f}{\Gamma_f + \Gamma_\nu} [1 - \exp(-\tau_i/t_\nu)] \quad \text{with}$$

$$\Gamma_f = \Gamma_f^{BW}(\sqrt{1 + \gamma^2} - \gamma), \quad (1)$$

where Γ_f^{BW} is the Bohr-Wheeler fission width and $\gamma = \beta/2\omega_0$ is the dissipation coefficient. ω_0 is the frequency of the harmonic oscillator defined by the inverted potential at the saddle point, t_ν is the mean particle decay time, and τ_i is defined as $\tau_i = \tau_f - \Sigma_{k=1}^{i-1} t_{\nu,k}$, i.e., the sum of the preceding particle decay times in the actual deexcitation cascade. The transient time or fission delay τ_f is

$$\tau_f = \begin{cases} \beta^{-1} \ln(10 B_f/T), & \beta \ll 2\omega_T \\ \beta(2\omega_T^2)^{-1} \ln(10 B_f/T), & \beta > 2\omega_T, \end{cases} \quad (2)$$

with $\omega_T = \omega_0 \approx 1 \times 10^{21}$ s^{-1} is the frequency of the harmonic oscillator oscillating the potential at the initial position, B_f is the fission barrier, and T is the temperature.

There exists a value of β around 2×10^{21} s^{-1} for which the transient time is minimum: for lower β, the coupling between the collective fission motion and the heat bath is weaker making the motion slower, while for larger β the motion is overdamped, two situations corresponding to the two cases of Eq. (2). This minimum transient time as a function of β is close to $(1-2) \times 10^{-21}$ s over most of the range in E^* explored in the present experiment.

The results of different ABLA calculations, for $\beta = 2 \times 10^{21}$ s^{-1}, 3×10^{21} s^{-1} and with the stationary Bohr-Wheeler approach are displayed in Fig. 20 for the Au and U targets. The a_f/a_n ratio has been taken according to the prescription of Ignatyuk *et al.* [66] that the authors of ABLA use as the default option [this ratio will be referred to as $(a_f/a_n)_{\text{Ign}}$ in the following]. In the calculation of the level density at the saddle point a_f, a surface term is added to the
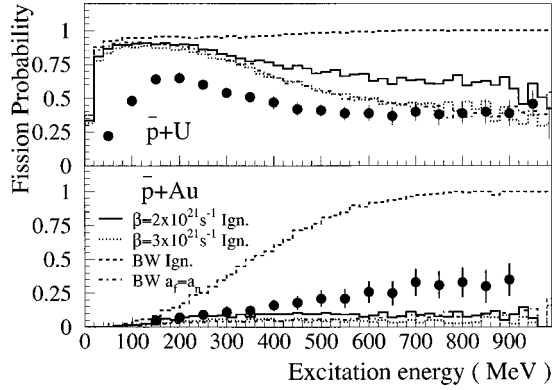
FIG. 20. Comparison between the experimental fission probability (circles) and the theoretical probabilities calculated with INC +ABLA (curves), for different values of β, or in the BW approach, and a_f/a_n.

volume term to account for the increase in level density resulting from the deformation. For the stationary Bohr-Wheeler case, the results corresponding to $a_f/a_n = 1$ are also shown. This calculation yields results very similar to those of GEMINI for the same a_f/a_n ratio as expected. Using $(a_f/a_n)_{\text{Ign}}$ with the stationary Bohr-Wheeler approach leads to a strong overestimate of P_{fis}, which is found to saturate at 1 for both targets at high E^*, in strong disagreement with the data. However, the combination of parameters (stationary case, $a_f/a_n = 1$) and $[\beta = 3 \times 10^{21} \text{ s}^{-1}, (a_f/a_n)_{\text{Ign}}]$ provide fairly similar reproduction of the data, although the fission probability for the Au is systematically underestimated by a factor of 2–3 as compared to the experimental data. As mentioned above, any finite value of β significantly different from 2×10^{21} s leads to a longer transient time and to a

sizable reduction of the fission probability. At least for Au, it appears that the only reasonable way to reach a better agreement with the data is to increase the a_f/a_n ratio, as had to be done with GEMINI (a fair reproduction being obtained with $a_f/a_n = 1.022$). It can be concluded from this comparison with the experimental data that the transient time has to be close to its lowest possible value in order to account for the large observed fission probabilities at high E^*. A similar conclusion has been obtained via the study of the isotopic dependence of the fission cross sections of different heavy nuclei at GSI [67].

It must be noted that the value of $\beta = 3 \times 10^{21} \text{ s}^{-1}$ is close to that found [68] to best reproduce the fission cross sections in relativistic heavy-ion collisions, $\beta = 1 \times 10^{21} \text{ s}^{-1}$ and those needed [15] to account for the prefission neutron multiplicities, $\beta \geq 2 \times 10^{21} \text{ s}^{-1}$.

The sensitivity of P_{fis} to the spin generated in the INC stage has also been investigated with ABLA. Increasing the spin predicted by the INC model by 30% leads to an increase by a factor close to 2 for the Au target over most of the E^* range, while there is an increase by 20% for the U target.

5. Fission probability: Dependence on the multiplicities of neutrons and LCPs

To go one step further, P_{fis} has also been studied as a function of the relative amount of detected neutrons and that of detected charged particles. Let us recall that these detected particles arise essentially from evaporation because of the low efficiency of the setup for high-energy particles. To our knowledge, this is the first time that P_{fis} can be investigated in such a systematic way.
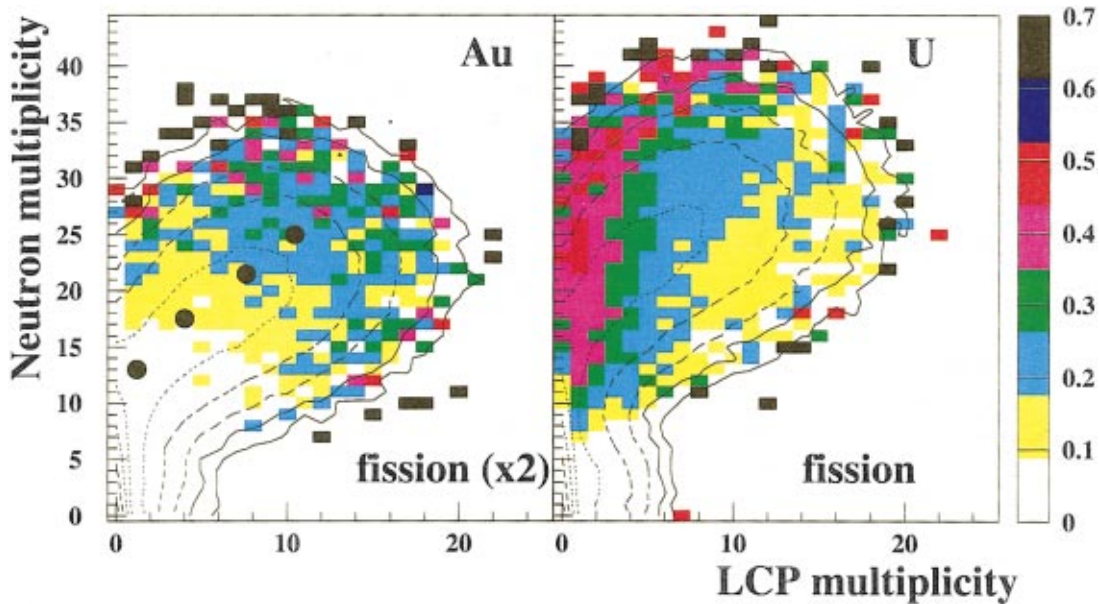

FIG. 21. (Color) Experimental fission probability (color scale) plotted as a function of the measured LCP and neutron multiplicities for Au and U. The total event yield is overlaid as contour lines (logarithmic scale, not shown, the factor between neighboring contour lines is 3.5). For Au, the four points correspond to the average location of the events with $E^* = 200$, 400, 600, and 800 MeV for increasing multiplicities, as calculated with the INC+GEMINI model.

The fission probability is plotted in Fig. 21 (color scale) as a function of M_n and M_{LCP} for the U and Au targets. The fission probability has been calculated as

$$P_{fis}(M_n,M_{LCP}) = \frac{Y_{fis}(M_n,M_{LCP})}{Y_{tot}(M_n,M_{LCP})}, \qquad (3)$$

where $Y_{fis}(M_n,M_{LCP})[Y_{tot}(M_n,M_{LCP})]$ is the fission (total) yield of events associated with the multiplicities M_n and M_{LCP}.

The event yield Y_{tot} is superimposed as contour lines in logarithmic scale (please note that the axes are interchanged as compared to Fig. 9). As was discussed in the context of Fig. 9, the position of the ridge of yield observed in this figure reflects the competition between neutrons and LCPs as the excitation energy increases (for illustration, the average location of the events with $E^* = 200–800$ MeV with 200-MeV steps, as calculated with the INC+GEMINI model, have also been depicted for Au). Consequently, iso-E^* curves correspond roughly to straight lines perpendicular to the ridge. Very different behaviors of P_{fis} are once more observed for the two targets. For the Au target, P_{fis} depends only a little on the relative amount of evaporated neutrons and LCPs. In sharp contrast, for the U target, P_{fis} displays a dramatic drop between the high-M_n region and the high-M_{LCP} one, at a constant E^*. Very interestingly, it is observed that the larger E^*, the larger the drop, which reaches a factor of about 5 for $E^* \simeq 1000$ MeV (high-multiplicity end of the ridge). One can quantify this effect via an ''apparent shift'' ΔM_n between the ridges of Y_{fis} and Y_{tot} at a constant M_{LCP}: for U, one finds $\Delta M_n \simeq 2$, while for Au $\Delta M_n \simeq 0$.

An experimental effect, namely a large variation of the detection efficiency with the FFs' atomic numbers, can be safely ruled out as an explanation for the behavior of P_{fis} observed for U: an estimate of this efficiency change leads to an upper limit of 20% for the variation in the FFs' atomic numbers considered here; moreover, the effect would be more pronounced for Au than for U as the charge lowering is more detrimental to the detection efficiency in the former case.

Figure 22 (top) displays the corresponding theoretical P_{fis} calculated as described in the previous section with $\tau_f = 0$ (without filtering with the setup acceptance). The trend exhibited by the data is reproduced for the two targets (ABLA also gives similar results in this respect, with the two sets of parameters mentioned at the end of the previous section).

This observation calls for two remarks.

(i) As shown in the previous section, the calculation predicts that the primary nuclei eventually undergoing fission are proton richer than average since their fissility is high. From this, it could be expected that the fission events are associated with more LCPs and fewer neutrons than average. The predictions actually exhibit the opposite trend, as seen in Fig. 22 (top). The large fraction of the particles emitted from the FFs in the calculation, as discussed in the context of Fig. 17, is responsible for this behavior. The FFs are indeed inherently neutron rich and decay via neutron emission even more predominantly than targetlike nuclei. The difference between the Au and U cases results from the curvature of the β-stability valley, making the FFs relatively neutron richer in the latter case (for a constant E^*). This effect can be further tested by plotting the same theoretical P_{fis} as a function of the multiplicities that would be obtained if all particles were emitted from the nucleus before scission (i.e., if the scission time were infinite). This is done in Fig. 22 (middle and bottom): for U, the extra neutrons associated with a finite Q_{eff} (see Ref. [15]) have been added for the pattern displayed in the middle panel, and omitted for the bottom panel (no friction). The number of extra neutrons decreases from 2 at low E^*, when the fissioning nucleus is close to U, to 0 when the fissioning nucleus' mass is lower than 218, i.e., around $E^* = 300$ MeV, taking into account the mass loss in the INC stage.

The patterns shown in Fig. 22 (middle and bottom) are very different from the experimental ones (Fig. 21) and the initial model predictions [Fig. 22 (top)], the fission events being now associated with more LCPs and fewer neutrons than average, as expected from the proton richness of the primary nuclei mentioned above.

(ii) The large emission from the FFs, crucial in the GEMINI calculation to account for the features displayed in Fig. 21, appears to contradict the conclusion, drawn from many earlier works involving the ''neutron-clock'' method [15], that the total E^* in the FFs is lower than 100 MeV regardless of the initial E^*. This contradiction may be only artificial as it can be conjectured that, in the limiting case of extreme deformation, the emission from the FFs is a reasonable approximation to the emission from the fissioning system before scission. The latter emission is not easy to model properly because of the uncertainties affecting the different parameters (level density parameter, transmission coefficients and binding energies) of the statistical model at large deformation and their constant change with time as the deformation increases. Our data can be explained *only* if either the above conjecture is correct or the FFs do really emit a large fraction of the particles, as assumed for technical reasons in statistical models like GEMINI or ABLA. Experimentally, the fraction of the evaporated particles emitted from the FFs in light-particle-induced reactions has been found and range between 80% [69] to 40% [59] using the correlation between the FF kinetic energies and the total mass loss, and close to 50% [61,70] with the ''neutron-clock'' method. These earlier measurements were all restricted to low E^* ($E^* < 200$ MeV). What becomes of this fraction at high E^* is an important issue for the understanding of the dynamics of fission induced by light particles. Depending on which of the above explanation prevails, our data could indicate that this fraction remains large at higher E^*.

This issue is discussed further in the next section.

6. Kinematical properties of particles accompanying fission

The emission patterns of the light particles in coincidence with the FFs also bring information on the fission process. The Galilei-invariant velocity distributions for the α particles emitted in reactions with the Au and U targets are plotted in
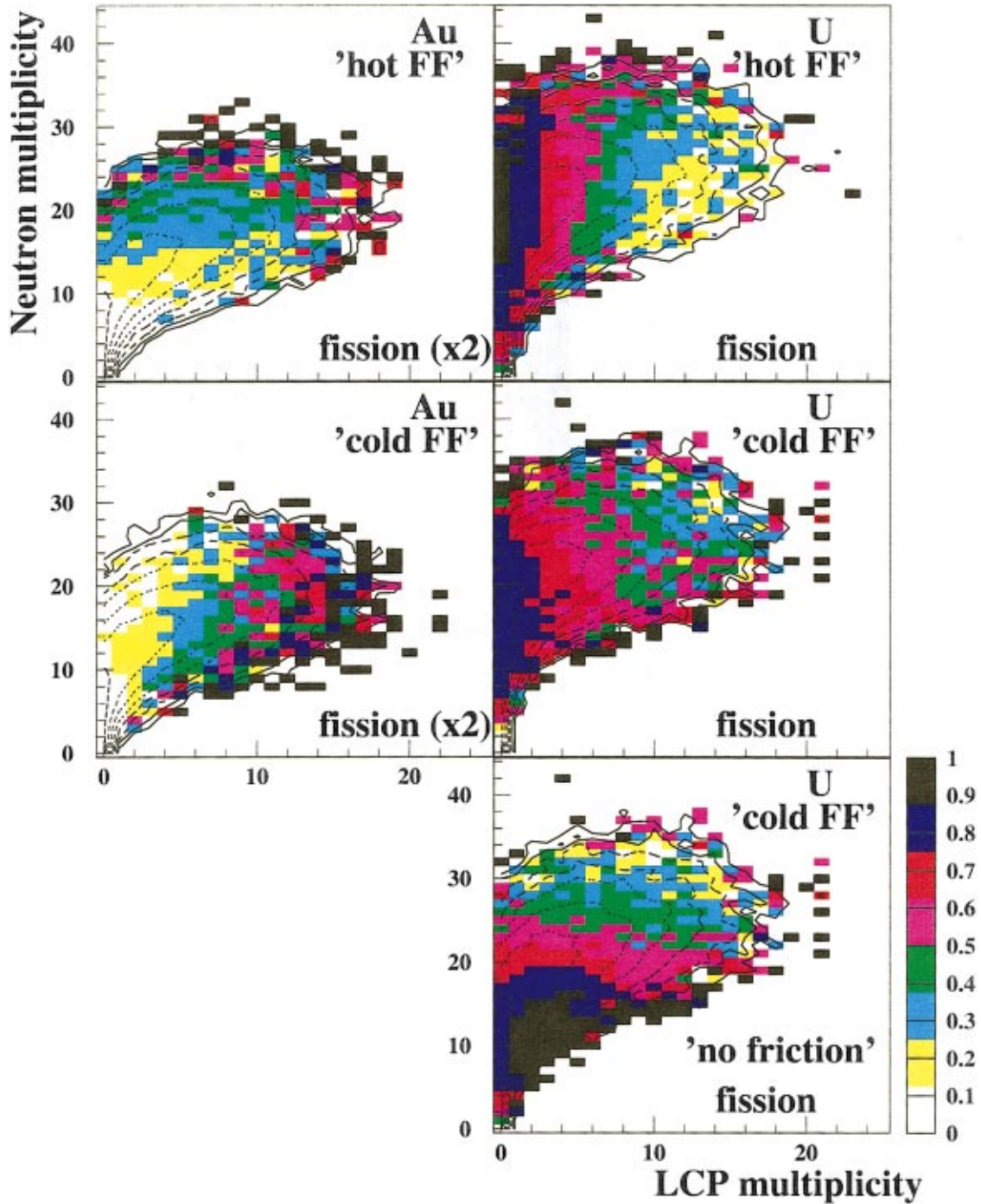
FIG. 22. (Color) Same as Fig. 21, but for theoretical fission probabilities calculated with GEMINI. The upper panels correspond to the standard GEMINI calculation leading to hot FFs, and the middle and lower ones to a modified calculation, in which the FFs are produced cold.

Fig. 23 as a function of the velocities parallel and perpendicular to the fission axis for three gates on the associated E^* (the positive axis points in the direction of the heaviest fragment by convention). The histograms depict the measured FF velocity distributions.

The velocity distributions displayed in Fig. 23 (already shown in Ref. [71]), corresponding to the Au and U targets respectively, exhibit circular patterns. For U with $E^* < 350$ MeV [Fig. 23 (right, upper panel)] the Coulomb ring is very well defined, indicating that the experimental acceptance

does not induce significant distortions. The ring becomes more and more smeared as E^* increases. For the Au target, it is already smeared at $E^* < 350$ MeV, a difference discussed below. Inspecting the distributions more closely reveals that the rings are actually somewhat asymmetric, with some additional yield on the light-fragment side at an angle of $\simeq 70°$ with respect to the velocity of the latter fragment (by 10% for U at large E^*). This asymmetry, combined with the observed smearing, points to a significant near-scission or postscission emission, although the large degree of isotropy
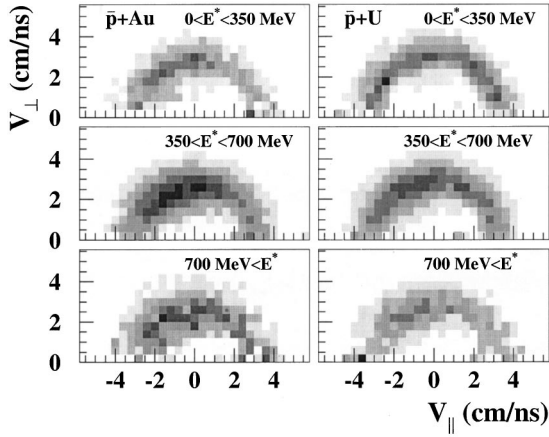
FIG. 23. Galilei-invariant velocity distributions of α particles plotted as a function of the velocity components parallel and perpendicular to the fission axis, the heavy-fragment velocity being directed in the positive direction, for the Au and the U targets.

of the ring seems to indicate that a large fraction of the particles are emitted before the FFs are fully accelerated. The larger smearing observed for Au than for U at $E^* < 350$ MeV might be a clue that fission takes place on a shorter time scale in the former case, as predicted by the calculations (Fig. 18) and leaves more excitation energy in the FFs.

Unfortunately, because of the present poor Z and A identification for the FFs, a more accurate estimation of the yield of the different emission components cannot be obtained with the present data. It is expected that this estimation will be possible with better quality data on proton-induced fission [52].

B. Intermediate-mass fragments

In the following, IMFs are defined as fragments with masses between 5 and 25. The IMF multiplicity (M_{IMF}) distribution has been investigated in order to characterize the nonfission events, exhausting the rest of the yield at a given E^*.

The experimental IMF distributions are displayed in Fig. 24 for different bins in the total light-particle multiplicity M_{LP} for the $\bar{p} + U$ reactions. These distributions assume similar Poisson-like shapes throughout the range of M_{LP} (the solid squares correspond to fitted Poisson distributions), with no clear indication for several components of distinct origins. This observation points to a unique dominant underlying process.

The mean IMF multiplicity $\langle M_{IMF} \rangle$ is plotted as a function of E^* in Fig. 25. It increases smoothly with E^* and reaches a value close to 1 for the highest E^* attained in the present experiment. The smoothness of the evolution again fortifies the conclusion that there is only one main process contributing. That the latter process is nothing else but evaporation can be justified on two grounds.

(i) IMF evaporation *must be present* just as LCP evaporation is, as soon as some sizable phase space exists for it. Although the IMF mass distribution could not be assessed with enough accuracy in the present experiment, the distri-
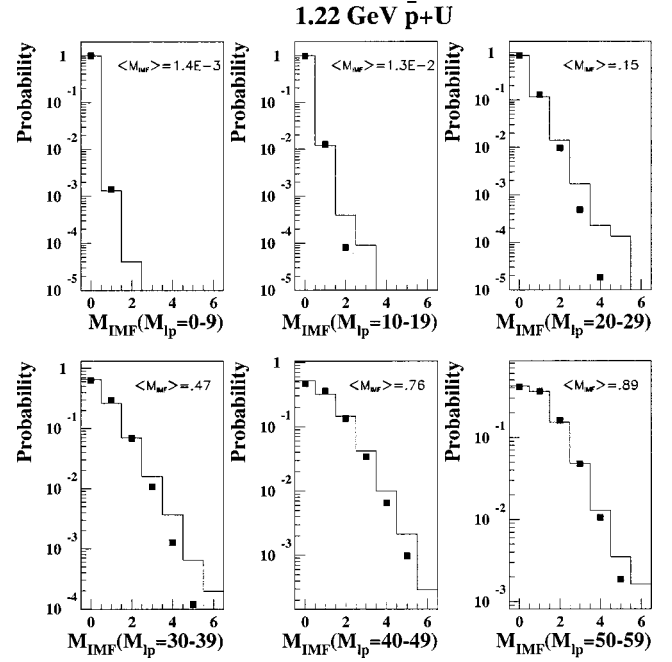

FIG. 24. Experimental IMF multiplicity distributions (histograms) measured for different bins in the associated total light-particle multiplicity. None of the multiplicities is corrected for efficiency. The symbols depict fitted Poisson distributions.

butions measured in proton-induced reactions [45] at similar excitation energies are peaked at very low masses, Li or Be being by far the most abundant IMFs.

(ii) From the low maximum $\langle M_{IMF} \rangle$, multifragmentation can be ruled out as a possible contender; even for the high-IMF multiplicity events the total mass carried off by IMFs does not comprise more than 30% of A_{target}, implying that a heavy residue subsists. At the highest E^*, events with $M_{IMF} \geq 3$ occur with a probability approaching only 5%.

These average IMF multiplicities can be compared with other data obtained for the same E^* range. Our value close to 1 at $E^* = 1$ GeV for Au is in reasonable agreement with that obtained by Sun *et al.* [42] ($\langle M_{IMF} \rangle \simeq 0.8$ at similar E^*) in Ar-induced reactions, who also concluded that multifragmentation is a rare process for E^* lower than 1 GeV.
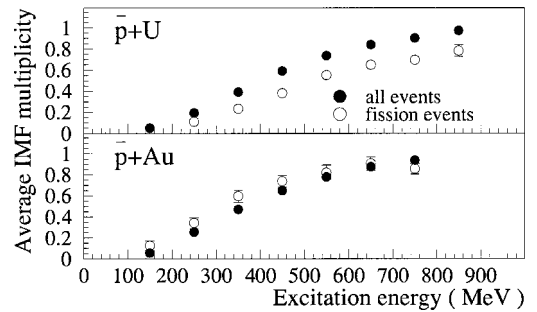

FIG. 25. Average IMF multiplicity plotted as a function of the initial excitation energy of the emitting nucleus, measured for all events (solid circles) and for the fission events (open circles) in the $\bar{p} + $ Au, U reactions.
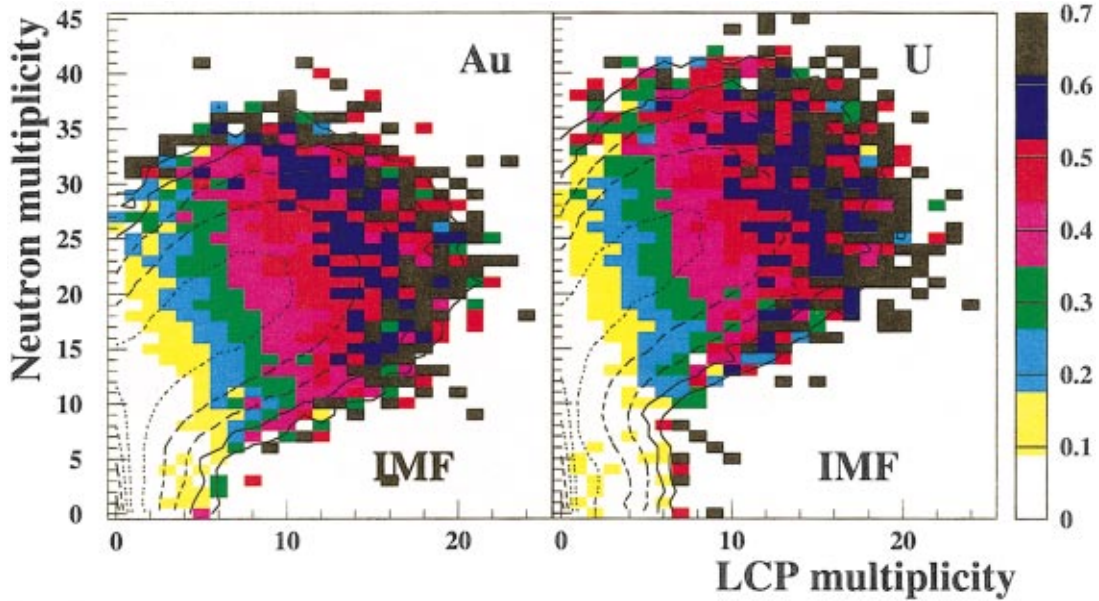
FIG. 26. (Color) Same as Fig. 21 but for the IMF-emission probability (color scale).

GEMINI does not provide M_{IMF} with the symmetric-fission option used for producing the results shown above. When used with the asymmetric-fission option, it predicts IMF multiplicities roughly consistent with those observed here (within 30%), but the fission data are then poorly produced (too large cross sections, by a factor of 2 for Au, and too broad FF mass distributions).

A few comments are needed concerning the averaging procedure used in this work and leading to the mean multiplicities displayed in Fig. 25. The excitation energy has been assessed event by event solely from the light-particle multiplicities, as described in Sec. IV B. This method assumes implicitly that the excitation energy consumed in emitting IMFs is low. To a large extent, the low multiplicities observed, as well as the dominance of light IMFs found in similar works, justify the validity of the above method. For the rare events associated with large IMF multiplicities, the above assumption may break down leading to an underestimation of E^* for these events. However, adding a sizable energy per emitted IMF to the estimated E^* would entail little changes in Fig. 25 except for the highest E^* ($E^* > 800$ MeV) where this procedure brings about a strong autocorrelation effect between E^* and M_{IMF}. The latter effect arises from the steep drop of the E^* distribution in the latter region. Since this region is dominated by fluctuations arising both from the statistical nature of the decay and the limited efficiency of the detector, assessing the physical behavior of the average IMF multiplicity in this region is impossible. Let us remark that the total E^* released via IMF emission amounts to a few tens of MeV only, while the resolution of the E^* determination is at least as large in the distribution tail. To avoid the autocorrelation problem, the course of action opted for in this paper is to present the IMF multiplicities as function of E^*, *as deduced from the light particle multiplicities*.

If instead of this method for determining E^*, the IMFs are included as done by the authors of Ref. [14], a steep increase of the IMF multiplicity is found for increasing E^*, reaching about 1.3 at 650 MeV and 3 at $E^* = 1$ GeV. These values are in close agreement with those given in Ref. [14], proving that no significant experimental discrepancy exists with the present work and emphasizing the above point that the observed $\langle M_{IMF}\rangle (E^*)$ relation depends crucially on the E^* determination method employed. In passing, one may also note that such a large IMF multiplicity of $\langle M_{IMF}\rangle = 3$ for $E^* = 1$ GeV brings up the problem as to why this multiplicity can be about three times greater in light-ion-induced reactions than in HI reactions [42], while it should be comparable if one is dealing with a pure thermal effect.

In Fig. 25 are also plotted the average IMF multiplicity observed in fission events. This multiplicity is observed to be slightly lower than the inclusive one at a given E^* for the U target, while no significant difference is visible for the Au target. This behavior may suggest an emission time for the IMFs shorter than the time needed to reach the saddle point, at least for U, the decrease in fissility associated with this emission leading to an hindrance of fission. Let us remark incidentally that these low IMF multiplicities justify the neglect of the IMF emission in interpreting the fission data in the previous section.

It is interesting to investigate how the IMF emission probability correlates with the relative multiplicities of evaporated neutrons and LCPs, along the line of the discussion of Fig. 21. The IMF emission probability is plotted as a function of the latter two multiplicities in Fig. 26, for the Au and U targets. The iso-IMF probabilities are straight lines almost perpendicular to the ridge observed in the yield distribution, i.e., very close to the iso-excitation energy lines mentioned above. This behavior proves that the IMF emission does not affect substantially the light-particle evaporation process, or in other words, that the competition between neutron and LCP emissions is not altered whether nuclei emit IMFs or otherwise. This conclusion confirms the absence of peculiarity in events associated with IMFs.
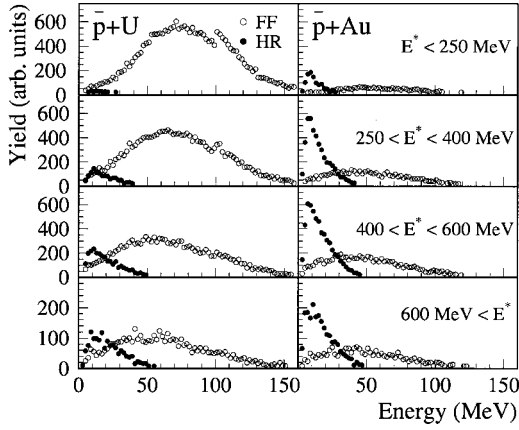
FIG. 27. Experimental kinetic-energy distributions of fission fragments (open symbols) and of heavy residues (solid symbols) for different bins in the excitation energy for $\bar{p}+$U, Au.

A comparison between Figs. 21 and 26 shows a striking difference for the U case, which proves that despite arbitrary mass cuts being applied for selecting the FFs, there is little contamination from the latter fragments in the selected IMFs.

C. Evaporation residues

From what precedes, it is expected that heavy residues survive in nonfission events regardless of the associated IMF multiplicity. As explained in the section devoted to the experimental method, an increasing fraction of these HRs with E^* have been detected. In Fig. 27 are compared the kinetic-energy distributions of the HRs and FFs for different bins in E^* for the Au and U targets. Although the mass calibration is uncertain for very heavy fragments, it has been possible to clearly distinguish the HR and FF components by requiring the total detected mass to be greater than 70% of the system mass, the fission events being associated with two coincident heavy fragments. The mere observation that the yield ratio between HR and FF evolves so strongly both with E^* and the target fissility proves that the two components do originate from distinct physical processes. HRs have also been observed in HI-induced reactions for a similar E^* range [42].

According to the INC calculations, these HRs are imparted only low momentum from the projectile during the INC stage, too low for these fragments to escape from the target foil with a sizable probability. However, the isotropic-recoil momentum gained during the evaporation stage broadens the HR momentum distribution considerably; the HRs associated with the high-momentum wing of this distribution becoming detectable.

An illustration of these effects is given in Fig. 28, displaying the experimental HR yield plotted as functions of the longitudinal (i.e., parallel to the beam) HR momentum and the sum of the longitudinal momenta of the detected charged fragments, i.e., both IMFs and LCPs, for different bins in the total IMF+LCP multiplicity. Two islands of yield are visible in this figure separated by a gap around $P_{||}=0$ stemming from the absorption in the target foil. The net excess of HRs in the forward direction is due to the recoil imparted during the INC stage, since the recoil in the evaporation stage is
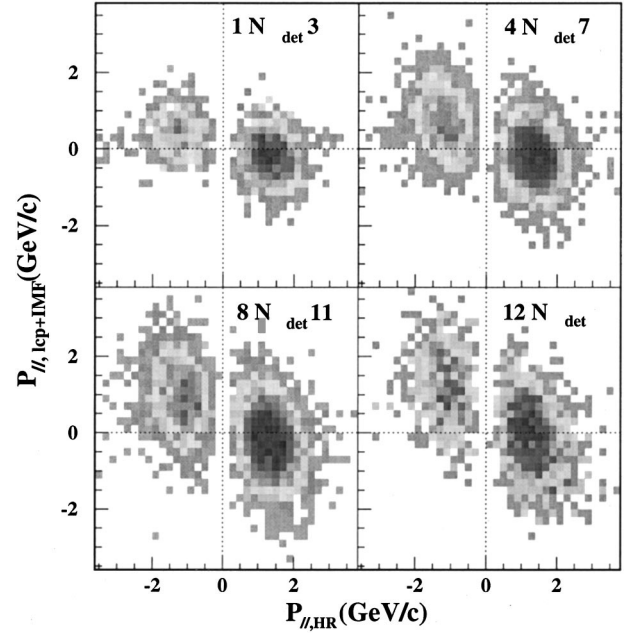

FIG. 28. Yield plotted as a function of the longitudinal momentum of the heavy residue and of the total longitudinal momentum carried by the detected charged particles and fragments, for different bins in the measured multiplicities, N_{det} of the latter.

isotropic. As expected, the total momentum $P_{||,HR}+\Sigma P_{||,cp}$ increases with the total multiplicity of charged fragments, i.e., with E^*, evidencing the increase in the momentum transfer. Figure 29 is equivalent to Fig. 28 for the transverse component of the momenta. The HR momentum and the total momentum carried by the charged fragments become increasingly antiparallel as E^* rises. This effect is a consequence of the decreasing share of the total recoil momentum taken up by the neutrons with increasing E^*. Figures 28 and
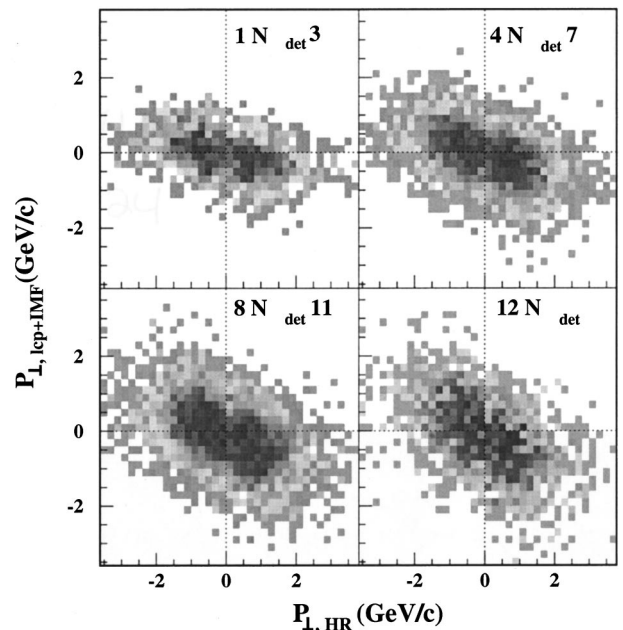

FIG. 29. Same as for Fig. 28 but for the transverse momenta.

29 prove that there is a strong kinematical bias affecting the HR detection, as mentioned above: this detection is made possible thanks to a fortuitous alignment of the emitted-particle momenta. Larger than average multiplicities of IMFs and LCPs also favor their detection since the charged-fragment emission imparts more momentum to the HR than the neutron emission.

Monte Carlo estimates of the HR detection efficiency, taking into account the primary-nuclei momentum distribution, the recoil gained during the evaporation stage, and the energy loss in the target foil lead to efficiencies ranging from 6% at $E^* = 200$ MeV to 35% at the highest E^*. Because of large uncertainties on these efficiencies, no direct, quantitative statements can be made from the observed HR yield. Furthermore, the strong selection bias affecting the detected HR makes the study of their experimental properties meaningless. The detection of HRs in substantial amounts allows nevertheless definite conclusions to be drawn on the competition between the reaction channels at play in these reactions. Events in which neither FFs nor HRs are detected, but only LCPs and IMFs, can safely be attributed to evaporation leading to nondetected HRs (except for a small contribution of fission in which none of the FFs is detected, representing about 5% of the fission events): should one or several lighter fragments have been produced, they would have been detected with a probability close to 70%. The observed HR yield, corrected for the efficiencies mentioned above, is in rough agreement with this expectation.

The observation of abundant HRs at the highest E^* found in this experiment confirms the picture established above via the investigation of fission and of the IMF production, namely that the nuclei retain conventional properties at E^* up to 4 MeV/nucleon. In particular, the observation of very heavy residues and fission fragments does not support the occurrence of a strong lowering of the density, either of dynamical origin or resulting from a thermal expansion. The latter effect was advocated in some recent works ([72] or [73] for an overview) on spallation reactions, with an almost linear decrease of the density for E^* below 500–700 MeV and a density equal to one-third of normal density for larger E^*.

The observation of low apparent Coulomb barriers in the IMF energy spectra has been interpreted [72] as manifesting the reduced density of the emitting source. The present results indicate that two alternative effects, neglected in the analysis of the above IMF spectra, lead to a smearing of these spectra and thus to an apparent lower Coulomb barrier. These effects comprise the possible emission from the FFs or from the ''neck'' connecting them before scission and the large recoil effects exemplified in Figs. 28 and 29. They should be taken into account when interpreting the fit of the IMF spectra with simple functions.

VI. SUMMARY

The annihilation of 1.22 GeV antiprotons has been used to excite nuclei, offering many interesting advantages over heavy-ion collisions. Theoretical calculations predict a fast direct stage, a limited loss of nucleons during this stage, little excitation of collective degrees of freedom and a single decaying nuclei. Another positive feature is the reliability and relative simplicity of the INC models describing the interaction of the pions within the nucleus. In order to take full benefit of these favorable conditions, a large-acceptance setup has been used, involving the simultaneous detection of neutrons and charged fragments with large efficiencies. A salient originality of this work concerns the acquisition trigger condition corresponding to the detection of the escaped charged pions, which unmistakably manifests the occurrence of an antiproton annihilation. All annihilation events have thus been recorded independently of the amount of excitation energy deposited into the target nuclei.

The experimental method employed offers two main advantages: (i) the excitation energy can be estimated event-by-event from the neutron and LCP multiplicities with an unprecedented accuracy of about 15% over most of the range, regardless of the decay channel and (ii) the relative probabilities of the different decay channels at play can be determined as a function of the excitation energy.

The power of annihilation of antiprotons in flight to form excited nuclei has first been investigated. The mean excitation energies are found to be about twice as large as those observed for annihilation of antiprotons at rest. The distributions extend up to 4–5 MeV/nucleon for the heaviest targets, in good agreement with the predictions of the INC model of Golubeva *et al.* [7].

Concerning the decay properties of the excited nuclei produced in the annihilation on the heaviest targets, the data analysis has been performed by trying to preserve the same line of minimum bias as in the data collection. A coherent picture has been obtained, embracing the full set of processes at play in the present reaction. The overwhelming prevalence of evaporation and fission up to $E^* = 4$ MeV/nucleon for reactions involving heavy targets like Au and U has been demonstrated. For the first time, the fission probability has been investigated as a function of E^* up to 4 MeV/nucleon providing insight into the dynamics of this process. In particular, a constraint on the transient time $\tau_f < 1 \times 10^{-21}$ s, has been established, which is about an order of magnitude lower than previous limits. The competition between the evaporation of neutrons and light-charged particles during the fission process has been studied for the first time. The large effect seen for U is interpreted as due to the large relative neutron richness of the FFs or of the elongated nucleus before scission. The velocity distributions of α particles associated with fission events also bring qualitative information on the scission time scale.

The average IMF multiplicity has been found to rise smoothly with E^* up to 1 at $E^* = 4$ MeV/nucleon. The multiplicity distributions are Poisson distributions to a good accuracy. No indication for the presence of another underlying process than evaporation has been observed, indicating that multifragmentation is still a very rare process at $E^* = 4$ MeV/nucleon.

The observation of large HR yields at high E^*, although made only possible by an accidentally large momentum buildup during the evaporation stage, bears out the picture established with the fission and IMF data. The data can be accounted for without evoking any substantial lowering in

the nuclear density, brought about by an expansion due to thermal pressure or by dynamical effects in the INC cascade. The present work illustrates the importance of experimentally addressing all decay channels at play to enable a comprehensive understanding of the properties of excited nuclei to emerge.

[1] P. Bonche, S. Levit, and D. Vautherin, Nucl. Phys. **A427**, 278 (1984); **A436**, 265 (1985).

[2] S. Levit and P. Bonche, Nucl. Phys. **A437**, 426 (1985).

[3] J. Cugnon, Nucl. Phys. **A462**, 751 (1987).

[4] J. Cugnon, P. Jasselette, and J. Vandermeulen, Nucl. Phys. **A470**, 558 (1987).

[5] J. Cugnon and J. Vandermeulen, Ann. Phys. (Paris) **14**, 49 (1989).

[6] A. S. Botvina, A. S. Iljinov, and I. N. Mishustin, Phys. Lett. B **205**, 421 (1988).

[7] Ye. S. Golubeva, A. S. Iljinov, A. S. Botvina, and N. M. Sobolevsky, Nucl. Phys. **A483**, 539 (1988).

[8] C. B. Dover, in *Proceedings of the Fourth LEAR Workshop*, Villars sur Ollon, Switzerland, 1987, edited by C. Amsler *et al.*, Nuclear Science Research Conference Series 14 (Harwood Academic, Chur, Switzerland, 1987), and references therein.

[9] M. R. Clover, R. M. Devries, N. J. DiGiacomo, and Y. Yariv, Phys. Rev. C **26**, 2138 (1982).

[10] P. L. McGaughey, M. R. Clover, and N. J. DiGiacomo, Phys. Lett. B **166**, 264 (1986).

[11] Yu. A. Batusov, S. A. Bunyatov, I. V. Falomkin, G. B. Pontecorvo, M. G. Sapoznikov, F. Balestra, S. Bossolasco, M. P. Bussa, L. Busso, L. Ferrero, D. Panzieri, G. Piragino, F. Tosello, C. Guaraldo, A. Maggiora, G. Bendiscioli, V. Filippini, A. Rotondi, A. Zenoni, and E. Lodi-Rizzini, Europhys. Lett. **2**, 115 (1986).

[12] S. Ahmad, B. E. Bonner, J. A. Buchanan, C. S. Chan, J. M. Clement, S. E. Eiseman, A. Empl, A. Etkin, K. J. Foley, R. W. Hackenburg, T. J. Hallman, M. A. Kramer, J. Kruk, S. J. Lindenbaum, R. S. Longacre, W. A. Love, L. Madansky, W. Morris, G. S. Mutchler, D. C. Peaslee, E. D. Platner, A. C. Saulys, and S. Toshkov, Nucl. Phys. **A558**, 393c (1993).

[13] T. Bressani, Nucl. Phys. **A558**, 415c (1993).

[14] L. Beaulieu, K. Kwiatkowski, W. C. Hsi, T. Lefort, L. Pienkowski, R. G. Korteling, G. Wang, B. Back, D. S. Bracken, H. Breuer, E. Cornell, F. Gimeno-Nogues, D. S. Ginger, S. Gushue, M. J. Huang, R. Laforest, W. G. Lynch, E. Martin, K. B. Morley, L. P. Remsberg, D. Rowland, E. Ramakrihnan, A. Ruangma, M. B. Tsang, V. E. Viola, E. Winchester, H. Xi, and S. J. Yennello, Phys. Lett. B **463**, 159 (1999).

[15] D. Hilscher and H. Rossner, Ann. Phys. (Paris) **17**, 471 (1992).

[16] F. Goldenbaum, M. Morjean, J. Galin, E. Liénard, B. Lott, A. Péghaire, Y. Périer, M. Chevallier, D. Dauvergne, R. Kirsch, J. C. Poizat, J. Rémilleux, C. Cohen, A. L'Hoir, G. Prévot, D. Schmaus, J. Dural, M. Toulemonde, and D. Jacquet, Phys. Rev. Lett. **82**, 5012 (1999).

[17] L. G. Moretto, K. X. Jing, R. Gatti, G. J. Wozniak, and R. P. Schmitt, Phys. Rev. Lett. **75**, 4186 (1995).

[18] F. Goldenbaum, W. Bohne, J. Eades, T. v. Egidy, P. Figuera, H. Fuchs, J. Galin, Ye. S. Golubeva, K. Gulda, F. J. Hartmann, D. Hilscher, A. S. Iljinov, U. Jahnke, J. Jastrzebski, W. Kurcewicz, B. Lott, M. Morjean, G. Pausch, A. Péghaire, L. Pienkowski, D. Polster, S. Proschitzki, B. M. Quednau, H. Rossner, S. Schmid, W. Schmid, and P. Ziem, Phys. Rev. Lett. **77**, 1230 (1996).

[19] S. Schmid, W. Schmid, F. J. Hartmann, T. v. Egidy, D. Hilscher, W. Bohne, P. Figuera, F. Goldenbaum, U. Jahnke, D. Polster, P. Ziem, J. Galin, B. Lott, M. Morjean, A. Péghaire, B. M. Quednau, K. Gulda, J. Jastrzebski, W. Kurcewicz, L. Pienkowski, G. Pausch, J. Eades, A. S. Iljinov, and M. V. Mebel, Z. Phys. A **359**, 27 (1997).

[20] U. Jahnke, W. Bohne, T. von Egidy, P. Figuera, J. Galin, F. Goldenbaum, D. Hilscher, J. Jastrzebski, B. Lott, M. Morjean, G. Pausch, A. Péghaire, L. Pienkowski, D. Polster, S. Proschitzki, B. M. Quednau, H. Rossner, S. Schmid, and W. Schmid, Phys. Rev. Lett. **83**, 4959 (1999).

[21] L. Pienkowski, W. Bohne, T. von Egidy, P. Figuera, J. Galin, F. Goldenbaum, D. Hilscher, U. Jahnke, J. Jastrzebski, B. Lott, M. Morjean, G. Pausch, A. Péghaire, D. Polster, S. Proschitzki, B. M. Quednau, H. Rossner, S. Schmid, and W. Schmid, Phys. Lett. B **472**, 15 (2000).

[22] D. Polster, D. Hilscher, H. Rossner, T. von Egidy, F. J. Hartmann, J. Hoffmann, W. Schmid, I. A. Pshenichnov, A. S. Iljinov, Ye. S. Golubeva, H. Machner, H. S. Plendl, A. Grochulska, J. Jastrzebski, W. Kurcewicz, P. Lubinski, J. Eades, and S. Neumaier, Phys. Rev. C **51**, 1167 (1995).

[23] L. Pienkowski, H. G. Bohlen, J. Cugnon, H. Fuchs, J. Galin, B. Gatty, B. Gebauer, D. Guerreau, D. Hilscher, D. Jacquet, U. Jahnke, M. Josset, X. Ledoux, S. Leray, B. Lott, M. Morjean, A. Péghaire, G. Röschert, H. Rossner, R. H. Siemssen, and C. Stéphan, Phys. Lett. B **336**, 147 (1994).

[24] W. Bauer, G. F. Bertsch, and H. Schulz, Phys. Rev. Lett. **69**, 1888 (1992).

[25] A. S. Iljinov, V. I. Nazaruk, and S. E. Chigrinov, Nucl. Phys. **A382**, 378 (1982).

[26] J. Pochodzalla, T. Möhlenkamp, T. Rubehn, A. Schüttauf, A. Wörner, E. Zude, M. Begemann-Blaich, Th. Blaich, H. Emling, A. Ferrero, C. Gross, G. Immé, I. Iori, G. J. Kunde, W. D. Kunze, V. Lindenstruth, U. Lynen, A. Moroni, W. F. J. Müller, B. Ocker, G. Raciti, H. Sann, C. Schwarz, W. Seidel, V. Serfling, J. Stroth, W. Trautmann, A. Trzcinski, A. Tucholski, G. Verde, and B. Zwieglinski, Phys. Rev. Lett. **75**, 1040 (1995).

[27] S. Bresson, M. Morjean, L. Pienkowski, R. Bougault, J. Colin, E. Crema, J. Galin, B. Gatty, A. Genoux-Lubain, D. Guerreau, D. Horn, D. Jacquet, U. Jahnke, J. Jastrzebski, A. Kordyasz, C. Le Brun, J. F. Lecolley, B. Lott, M. Louvel, C. Paulot, E.

Piasecki, J. Pouthas, B. M. Quednau, W. U. Schröder, E. Schwinn, W. Skulski, and J. Töke, Phys. Lett. B **294**, 33 (1992).

[28] GEMINI code obtained via ftp from wunmr.wustl.edu—see R. J. Charity, M. A. McMahan, G. J. Wozniak, L. G. Moretto, D. G. Sarantites, L. G. Sobotka, G. Guarino, A. Pantaleo, L. Fiore, A. Gobbi, and K. D. Hildenbrand, Nucl. Phys. **A483**, 371 (1988).

[29] P. Figuera, W. Bohne, B. Drescher, F. Goldenbaum, D. Hilscher, U. Jahnke, B. Lott, L. Pienkowski, and P. Ziem, Z. Phys. A **352**, 315 (1995).

[30] J. Galin and U. Jahnke, J. Phys. G **20**, 1105 (1994).

[31] DENIS, a computer code developed by J. Poitou and C. Signarbieux, Nucl. Instrum. Methods **114**, 113 (1974).

[32] M. Ogihara, Y. Nagashima, W. Galster, and T. Mikumo, Nucl. Instrum. Methods Phys. Res. A **251**, 313 (1986).

[33] H.-O. Neidel and H. Henschel, Nucl. Instrum. Methods **178**, 137 (1980).

[34] W. Bohne *et al.*, Nucl. Instrum. Methods Phys. Res. A **240**, 145 (1985).

[35] H. P. Wellisch and D. Axen, Phys. Rev. C **54**, 1329 (1996); revised by R. E. Prael and M. B. Chadwick, Addendum to Applications of evaluated nuclear data in the Lahet^TM code, Report No. LA-UR-97-1745.

[36] M. Enke, C. M. Herbach, D. Hilscher, U. Jahnke, O. Schapiro, A. Letourneau, J. Galin, F. Goldenbaum, B. Lott, A. Péghaire, D. Filges, R. D. Neef, N. Paul, H. Schaal, and L. Pienkowski, Nucl. Phys. **A657**, 317 (1999).

[37] H. Aihara, J. Chiba, H. Fujii, T. Fujii, H. Iwasaki, T. Kamae, K. Nakamura, T. Sumiyoshi, Y. Takada, T. Takeda, M. Yamauchi, and H. Fukuma, Nucl. Phys. **A360**, 291 (1981).

[38] J. Töke, B. Lott, S. P. Baldwin, B. M. Quednau, W. U. Schroeder, L. G. Sobotka, J. Barreto, R. J. Charity, D. G. Sarantites, D. W. Tracener, and R. T. de Souza, Phys. Rev. Lett. **75**, 2920 (1995).

[39] GEANT, CERN Program Library long writeup W5013, 1993 (unpublished).

[40] E. Piasecki, S. Bresson, B. Lott, R. Bougault, J. Colin, E. Crema, J. Galin, B. Gatty, A. Genoux-Lubain, D. Guerreau, D. Horn, D. Jacquet, U. Jahnke, J. Jastrzebski, A. Kordyasz, C. Le Brun, J. F. Lecolley, M. Louvel, M. Morjean, C. Paulot, L. Pienkowski, J. Pouthas, B. M. Quednau, W. U. Schröder, E. Schwinn, W. Skulski, and J. Töke, Phys. Rev. Lett. **66**, 1291 (1991).

[41] T. von Egidy, P. Figuera, J. Galin, F. Goldenbaum, Ye. S. Golubeva, M. Hasinof, D. Hilscher, A. S. Iljinov, U. Jahnke, M. Krause, W. Kurcewicz, X. Ledoux, B. Lott, L. Maier, M. Manrique de Lara, G. Pausch, L. Pienkowski, B. M. Quednau, W. Schott, W. U. Schröder, and J. Töke, Eur. Phys. J. A **8**, 197 (2000).

[42] E. Colin *et al.*, Phys. Rev. C **57**, R1032 (1998); R. Sun *et al.*, Phys. Rev. Lett. **84**, 43 (2000); Phys. Rev. C **61**, 061601 (2000); E. Colin *et al.*, *ibid.* **61**, 067602 (2000).

[43] J. A. Hauger *et al.*, Phys. Rev. Lett. **77**, 235 (1996).

[44] G. Wang, K. Kwiatkowski, V. E. Viola, W. Bauer, and P. Danielewicz, Phys. Rev. C **53**, 1811 (1996).

[45] X. Ledoux, H. G. Bohlen, J. Cugnon, H. Fuchs, J. Galin, B. Gatty, B. Gebauer, D. Guerreau, D. Hilscher, D. Jacquet, U. Jahnke, M. Josset, S. Leray, B. Lott, M. Morjean, B. M. Qued-

nau, G. Röschert, H. Rossner, A. Péghaire, L. Pienkowski, R. H. Siemssen, and C. Stéphan, Phys. Rev. C **57**, 2375 (1998).

[46] J. B. Cumming, P. E. Haustein, T. J. Ruth, and G. J. Virtes, Phys. Rev. C **17**, 1632 (1978).

[47] K. Nakai, T. A. Shibata, S. Enmyo, S. Sasaki, M. Sekimoto, I. Arai, K. Nakayama, K. Ichimaru, H. Nakamura-Yokota, and R. Chiba, Phys. Lett. B **121**, 373 (1983).

[48] W. C. Hsi, K. Kwiatkowski, G. Wang, D. S. Bracken, E. Cornell, D. S. Ginger, V. E. Viola, N. R. Yoder, R. G. Korteling, F. Gimeno-Nogures, E. Ramakrishnan, D. Rowland, S. J. Yenello, M. J. Huang, W. G. Lynch, M. B. Tsang, H. Xi, Y. Y. Chu, S. Gushue, L. P. Remsberg, K. B. Morley, and H. Breuer, Phys. Rev. Lett. **79**, 817 (1997).

[49] D. Hilscher, U. Jahnke, F. Goldenbaum, L. Pienkowski, J. Galin, and B. Lott, Nucl. Instrum. Methods Phys. Res. A **414**, 100 (1998).

[50] L. Pienkowski, F. Goldenbaum, D. Hilscher, U. Jahnke, J. Galin, and B. Lott, Phys. Rev. C **56**, 1909 (1997).

[51] J. Jastrzebski, W. Kurcewicz, P. Lubinski, A. Grabowska, A. Stolarz, H. Daniel, T. von Egidy, F. J. Hartmann, P. Hofmann, Y. S. Kim, A. S. Botvina, Ye. S. Golubeva, A. S. Iljinov, G. Riepe, and H. S. Plendl, Phys. Rev. C **47**, 216 (1993).

[52] Preliminary data by the NESSI collaboration (unpublished).

[53] J. Cugnon, University of Liége, Preprint No. ULG. PNT. 93. 1G (unpublished).

[54] J. J. Gaimard and K.-H. Schmidt, Nucl. Phys. **A531**, 709 (1991).

[55] J. Hudis and S. Katcoff, Phys. Rev. C **13**, 1961 (1976).

[56] G. Klotz-Engmann, H. Oeschler, J. Stroth, E. Kankeleit, Y. Cassagnou, M. Conjaud, R. Dayras, S. Harar, R. Legrain, E. C. Pollacco, and C. Volant, Nucl. Phys. **A499**, 392 (1989).

[57] G. Rémy, J. Ralarosy, R. Stein, M. Debeauvais, and J. Tripier, Nucl. Phys. **A163**, 583 (1971).

[58] M. Thoennessen, J. R. Beene, F. E. Bertrand, C. Barktash, M. L. Halbert, D. J. Horen, D. C. Hensley, D. G. Sarantites, W. Spang, D. W. Stracener, and R. L. Varner, Phys. Lett. B **282**, 288 (1992).

[59] P. Hofmann, A. S. Iljinov, Y. S. Kim, M. V. Mebel, H. Daniel, P. David, T. von Egidy, T. Haninger, F. J. Hartmann, J. Jastrzebski, W. Kurcewicz, J. Lieb, H. Machner, H. S. Plendl, G. F. Riepe, B. Wright, and K. Ziock, Phys. Rev. C **49**, 2555 (1994).

[60] Y. S. Kim, A. S. Iljinov, M. V. Mebel, P. Hofmann, H. Daniel, T. von Egidy, T. Haninger, F. J. Hartmann, H. Machner, H. S. Plendl, and G. F. Riepe, Phys. Rev. C **54**, 2469 (1996).

[61] W. Schmid, T. von Egidy, F. J. Hartmann, J. Hofmann, S. Schmid, D. Hilscher, D. Polster, H. Rossner, A. S. Iljinov, M. V. Mebel, D. I. Ivanov, V. G. Nedozorov, A. S. Sudov, H. Machner, H. S. Plendl, J. Eades, and S. Neumaier, Phys. Rev. C **55**, 2965 (1997).

[62] B. D. Wilkins, S. B. Kaufman, E. P. Steinberg, J. A. Urbon, and D. J. Henderson, Phys. Rev. Lett. **43**, 1080 (1979).

[63] L. N. Andronenko, A. A. Kotov, M. M. Nesterov, V. F. Petrov, N. A. Tarasov, L. A. Vaishene, and W. Neubert, Z. Phys. A **318**, 97 (1984).

[64] N. Bohr and J. A. Wheeler, Phys. Rev. **56**, 426 (1939).

[65] P. Grangé, Nucl. Phys. **A428**, 37c (1984).

[66] A. V. Ignatyuk, M. G. Itkis, V. N. Okolovitch, G. N. Smirekin, and A. S. Tishin, Yad. Fiz. **21**, 1185 (1975) [Sov. J. Nucl. Phys. **21**, 612 (1975)].

[67] A. Heinz, B. Jurado, J. Benlliure, C. Böckstiegel, H.-G. Clerc, A. Grewe, M. de Jong, A.R. Junghans, J. Müller, K.-H. Schmidt, and S. Steinhäuser, GSI Annual Report, 1999 (unpublished).

[68] A. V. Ignatyuk, G. A. Kudyaev, A. Junghans, M. de Jong, H.-G. Clerc, and K.-H. Schmidt, Nucl. Phys. **A593**, 519 (1995).

[69] Yu. A. Chestnov, A. V. Kravtsov, B. Yu. Sokolovski, and G. E. Solyakin, Sov. J. Nucl. Phys. **45**, 11 (1987).

[70] Z. Fraenkel, A. Breskin, R. Chechik, S. Wald, R. Abbeg, H. W. Fielding, P. Kitching, S. T. Lam, G. C. Neilson, W. C. Olsen, and J. Uegaki, Phys. Rev. C **41**, 1050 (1990).

[71] L. Pienkowski, W. Bohne, T. von Egidy, P. Figuera, J. Galin, F. Goldenbaum, D. Hilscher, U. Jahnke, J. Jastrzebski, B. Lott, M. Morjean, G. Pausch, A. Péghaire, D. Polster, S. Proschitzki, B. M. Quednau, H. Rossner, S. Schmid, and W. Schmid, in *Proceedings of LEAP'98*, edited by C. Cicalo, A. de Falco, G. Puddu, and S. Serci [Nucl. Phys. **A655**, 269c (1999)].

[72] E. Renshaw Foxford, K. Kwiatkowski, D. S. Bracken, K. B. Morley, V. E. Viola, N. R. Yoder, C. Volant, E. C. Pollacco, R. Legrain, R. G. Korteling, W. A. Friedman, J. Brzynchczyk, and H. Breuer, Phys. Rev. C **54**, 749 (1996).

[73] V. Viola and K. Kwiatkowski, Am. Sci. **86**, 449 (1998), and references therein.